The Astrophysical Journal, 954:30 (22pp), 2023 September 1 https://doi.org/10.3847/1538-4357/acd7eb

The Temporal and Spatial Evolution of Magnetohydrodynamic Wave Modes in Sunspots

A. B. Albidah[1], V. Fedun[2], A. A. Aldhafeeri[3], I. Ballai[4], D. B. Jess[5,6], W. Brevis[7], J. Higham[8], M. Stangalini[9], S. S. A. Silva[2], C. D. MacBride[5], and G. Verth[4]

[1] Department of Mathematics, College Of Science, Majmaah University, Al-Majmaah 11952, Saudi Arabia; a.albedah@mu.edu.sa
[2] Plasma Dynamics Group, Department of Automatic Control and Systems Engineering, The University of Sheffield, Mappin Street, Sheffield, S1 3JD, UK
[3] Mathematics and Statistic Department, Faculty of Science, King Faisal University, Al-Hassa, P.O. Box 400, Hofuf 31982, Saudi Arabia
[4] Plasma Dynamics Group, School of Mathematics and Statistics, The University of Sheffield, Hicks Building, Hounsfield Road, Sheffield, S3 7RH, UK
[5] Astrophysics Research Centre, School of Mathematics and Physics, Queen's University Belfast, Belfast, BT7 1NN, UK
[6] Department of Physics and Astronomy, California State University Northridge, Northridge, CA 91330, USA
[7] School of Engineering, Pontificia Universidad Católica de Chile, Chile
[8] School of Environmental Sciences, Department of Geography and Planning, University of Liverpool, Roxby Building, Liverpool, L69 7ZT, UK
[9] ASI, Italian Space Agency, Via del Politecnico snc, I-00133 Rome, Italy

Received 2022 August 1; revised 2023 May 10; accepted 2023 May 21; published 2023 August 21

Abstract

Through their lifetime, sunspots undergo a change in their area and shape and, as they decay, they fragment into smaller structures. Here, for the first time we analyze the spatial structure of the magnetohydrodynamic (MHD) slow-body and fast-surface modes in the observed umbrae as their cross-sectional shape changes. The proper orthogonal decomposition (POD) and dynamic mode decomposition (DMD) techniques were used to analyze 3 and 6 hr Solar Dynamics Observatory/Helioseismic and Magnetic Imager time series of Doppler velocities at the photospheric level of approximately circular and elliptically shaped sunspots. Each time series was divided into equal time intervals to evidence the change in the shape of the sunspots. To identify the physical wave modes, the POD/DMD modes were cross-correlated with a slow-body mode model using the exact shape of the umbra, whereas the shape obtained by applying a threshold level of the mean intensity for every time interval. Our results show that the spatial structure of MHD modes are affected, even by apparently small changes in the umbral shape, especially in the case of the higher-order modes. For the data sets used in our study, the optimal time intervals to consider the influence of the change in the shape on the observed MHD modes is 37–60 minutes. The choice of these intervals is crucial to properly quantify the energy contribution of each wave mode to the power spectrum.

Unified Astronomy Thesaurus concepts: Sunspots (1653); Radiative magnetohydrodynamics (2009); Emerging flux tubes (458); Wavelet analysis (1918); Solar coronal waves (1995); Active solar chromosphere (1980); Penumbra (1205); Umbra (1744)

1. Introduction

One of the most rapidly evolving fields in solar physics is the study of magnetohydrodynamic (MHD) waves and oscillations in the solar atmosphere. Waves observed with high accuracy in various wavelengths make it possible to diagnose plasma parameters, e.g., density, temperature, chemical composition, and heating/cooling functions, and analyze the magnetic field structure and magnitude. Sunspots support a large variety of MHD waves propagating along and across the magnetic field, making them an ideal location for studying MHD waves given their stability, a relatively simple magnetic configuration that can be observed, and long lifetime (Jess et al. 2015; Khomenko & Collados 2015; Albidah et al. 2021, 2022; Stangalini et al. 2021, 2022, to name but a few).

The high-resolution observations of sunspots and the dynamics associated with these magnetic features also allow investigation the effect of particular shapes of the cross sections of the sunspots on the nature and morphology of waves. Theoretical models provide a relatively accurate behavior of MHD waves in the magnetic waveguides with simple geometry, i.e., approximately circular (for conciseness, from this point on we will refer to that sunspot as "circular"), and to a lesser extent, approximately elliptical ("elliptical") cross sections, and observations seem to recover rather well these properties. However, so far very few studies were dedicated to the theoretical study of MHD modes in waveguides with arbitrary shapes. The identification and analysis of MHD modes in the observations are a challenging problem as well. In fact, current studies assume a stationary magnetic waveguide for the duration of observation. While this assumption is valid for short-lived or transient modes, for waves with characteristic lifetimes comparable to the rate of change in the shape and dynamical/thermodynamical state of the waveguide, these changes might become important. Recently, Albidah et al. (2022) found that higher-order MHD modes and higher harmonics in the umbral regions of sunspots are strongly affected by the shape of the waveguide. Using the proper orthogonal decomposition (POD; Pearson 1901) and the dynamic mode decomposition (DMD; Schmid 2010) analyses of the average umbral shapes, the study by Albidah et al. (2022) was one of the first investigations to identify the presence of higher-order modes in sunspots.

The POD and DMD techniques have been widely applied to investigate periodic changes in fluids (i.e., Murray & Ukeiley 2007; Rowley et al. 2009; Bagheri 2013; Jovanović et al. 2014; Berry et al. 2017). POD assumes orthogonality in space and offers clear ranking criteria based on the contribution of modes to the total variance of the signal. In contrast, DMD assumes orthogonality in time, which means that different

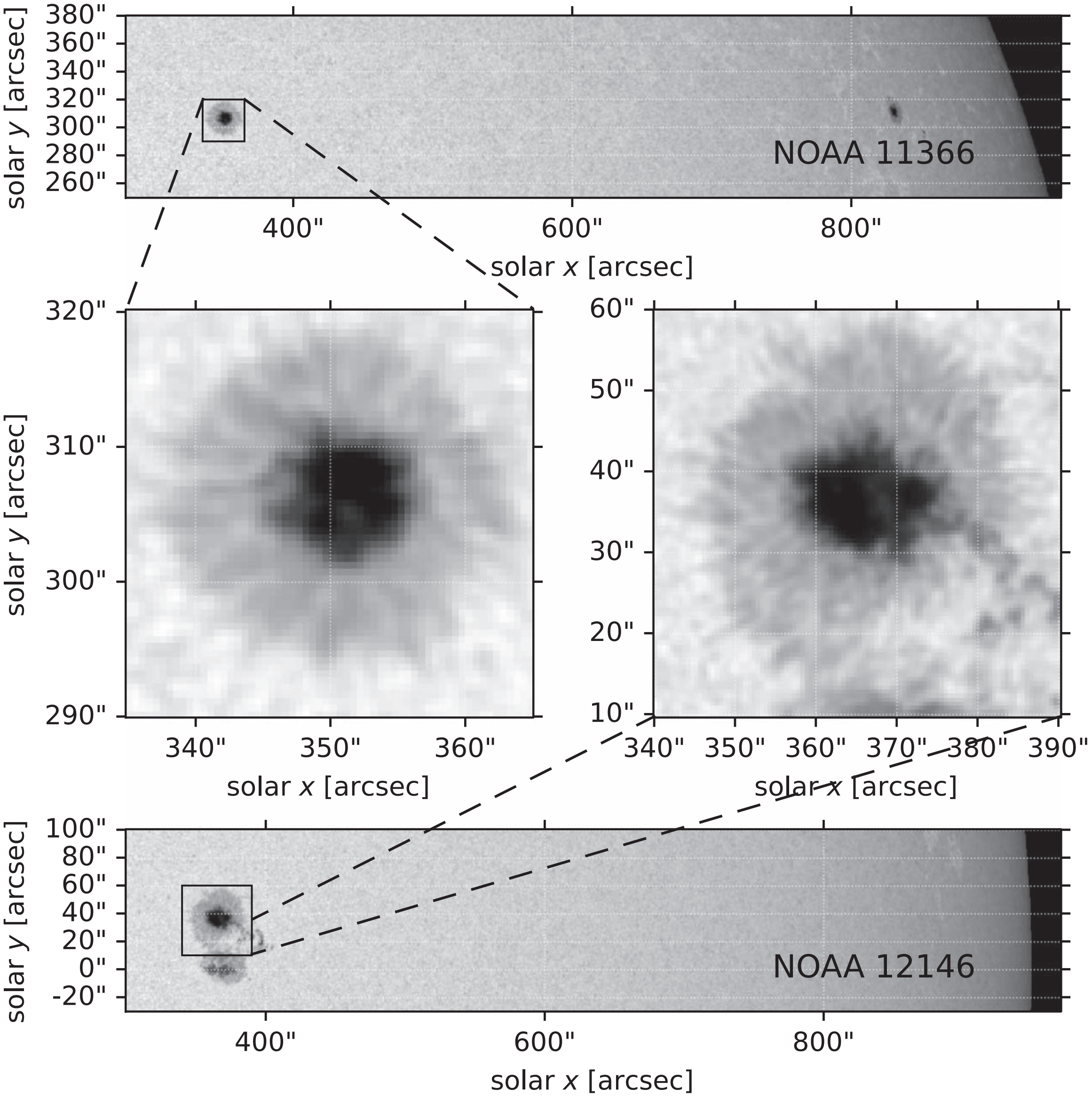

Figure 1. Continuum intensity images from SDO/HMI observations of two different sunspots. The sunspot location on the solar disk during the period of observation is identified with a black rectangle in the top and bottom panels for active regions NOAA 11366 and NOAA 12146, respectively. Magnified views of the NOAA 11366 circular cross section sunspot and the NOAA 12146 elliptical cross section sunspot are shown in the middle left and right panels, respectively.

modes cannot have identical frequencies. POD and DMD can be used together to reveal temporally and spatially orthogonal features in solar observations by following the approach developed by Higham et al. (2018). When applied to investigate MHD waves, POD and DMD disentangle the signals and separate the oscillating pattern resulting from wave propagation. Previous investigation employing the combined POD/DMD techniques (Albidah et al. 2021, 2022) on solar physics data assumed that the umbral boundary does not change, which is an idealistic approach. In reality, extended high-resolution observations show that the boundary between a sunspot umbra and its penumbra is not stationary; instead its shape can change in time.

In this work, we study the effect of the change in the shape of the umbral boundary on the nature and morphology of waves identified by applying the POD and DMD techniques on Doppler velocity data sets of two distinct sunspots. The identified modes are compared with the model of the irregular shape that corresponds to the realistic shape of the sunspot; the model has been described in the works of Albidah et al. (2022) and Stangalini et al. (2022).

2. Observations

The data used in this study, the continuum intensity and Doppler velocity, were obtained from observations by the Helioseismic and Magnetic Imager (HMI; Schou et al. 2011) on board the Solar Dynamics Observatory (SDO; Pesnell et al. 2011).

The two active regions each contain a sunspot with an approximately circular and elliptical cross-sectional shape, respectively. Data for NOAA 11366 were acquired from 15:00 to 18:00 UT on 2011 December 10, while data for NOAA 12146 were acquired from 10:00 to 16:00 UT on 2014 August 24. The cadence of the measurements was 45 s, which provided 241 images (∼3 hr) of NOAA 11366 and 481 images (∼6 hr) of NOAA 12146 for both the continuum intensity and the Doppler velocity. The spatial sampling of all

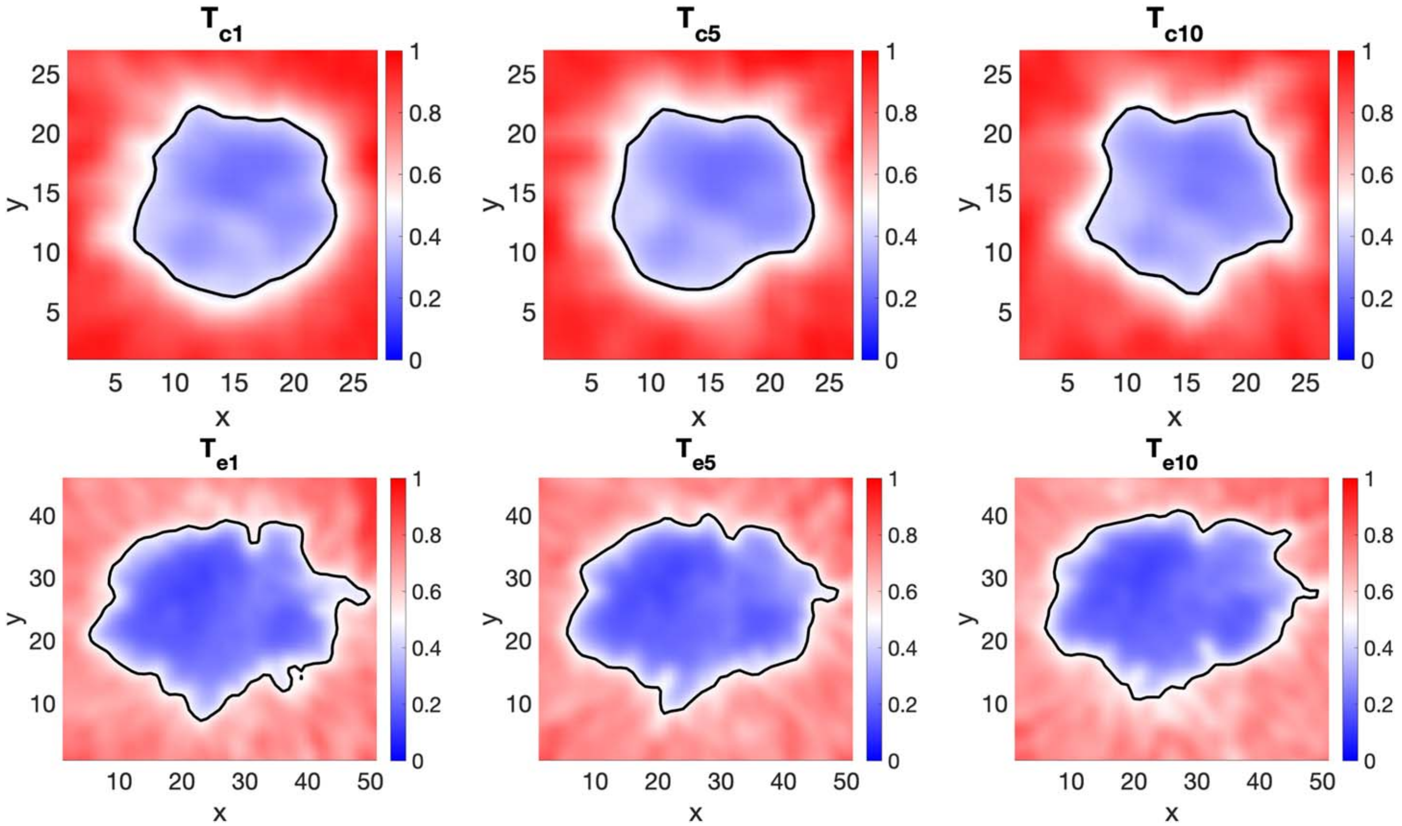

Figure 2. The mean of the continuum intensity time series for three different time intervals for each sunspot is shown for the approximately "circular" sunspot, NOAA 11366, at T_{c1}, T_{c5}, and T_{c10} (upper panels) and the 'elliptical" sunspot, NOAA 12146, at T_{e1}, T_{e5}, and T_{e10} (lower panels). The color bar displays the magnitude of the mean time series for each time interval. The umbra/penumbra boundary was obtained by taking threshold levels for both sunspots and is indicated in black. The spatial scale is given in pixels (one pixel is equal to $0\overset{''}{.}504$, which is approximately 356 km on the surface of the Sun).

the data products was $0\overset{''}{.}504$ per pixel, which is approximately 356 km on the surface of the Sun.

To account for the rotation of the Sun relative to SDO, the observations of the two active regions were reprojected to the reference frame of an Earth-based observer at 15:00 UT and 10:00 UT, respectively, on the same date each active region was observed. The reprojection was carried out using Version 3.0.0 (Mumford et al. 2021) of the SunPy open-source software package (The SunPy Community et al. 2020). The pixel values of each image are mapped to the new projection and interpolated using a nearest-neighbor algorithm. The motion of the center of the Sun is ignored such that coordinates are always relative to the center of the Sun. Figure 1 shows the sunspots used in this study and identifies their position on the solar disk as would be seen by an Earth-based observer.

3. Analysis and MHD Wave Mode Identification

The selected sunspots present changes in their umbral cross-sectional shape over the time interval used for our analysis: 3 and 6 hr for the circular and elliptical sunspots, respectively. In order to facilitate the temporal analysis of the modification in the shape of cross section, we divide the time-series data of both sunspots into 10 time intervals (T_{ci} and T_{ei}). Here, indexes c and e are used to distinguish between the time intervals of the circular and elliptical sunspots, and $i = 1...10$ corresponds to the 10 separate time intervals. In the case of the circular sunspot, every time interval contains 50 images (∼37.5 minutes) and it is overlapped with the previous time interval by 20 images (∼15 minutes). Thus, the time interval T_{ci+1} is 20 images ahead of the time interval T_{ci}. For the elliptical sunspot, every time interval contains 80 images (∼60 minutes), and they are overlapped with the previous time interval by 40 images (∼30 minutes), i.e., time interval T_{ei+1} is 40 images ahead of the time interval T_{ei}. For both sunspots, the width of the time intervals was chosen to cover, at least, 5 times the typical period of oscillations, which varies with height, from 5 to 3 minutes, from the photosphere to the chromosphere, respectively (see Nagashima et al. 2007; Stangalini et al. 2011, 2021; Jess et al. 2012; Khomenko & Collados 2015).

The boundaries between the umbra and penumbra were constructed by computing the average intensity for every time interval and then applying intensity threshold levels. Accordingly, in the case of the circular sunspot we set this intensity level at 0.45, while in the case of the elliptical sunspot we adopted the level at 0.5. Thereby, for each time interval the umbra boundary will have a different shape, as illustrated in Figure 2 for three different time intervals.

To obtain the theoretical umbral slow-body wave modes we use the observed irregular cross-sectional shape, as was done previously by Stangalini et al. (2022) and Albidah et al. (2022). This allows us to accurately correlate the modes in the observational data with their theoretical counterparts. The governing Helmholtz-type equation for the vertical velocity perturbation solved by us (see Equation (14) in Albidah et al. 2022) does not assume any long or short wavelength limits and is therefore valid for arbitrary wavelengths. As was done previously by Stangalini et al. (2022) and Albidah et al. (2022),

Table 1
Summary of Possible MHD Modes Observed in the Circular Sunspot in the Selected Time Intervals

M_i	T_{ci}	POD	Peaks of PSD (mHz)	DMD (mHz)	MHD Mode Observed
M_1	T_{c3}	4	3.5 and 4.4	3	FSBS ($n = 0$)
M_1	T_{c4}	4	3.5 and 4.4	3.4	FSBS ($n = 0$)
M_1	T_{c5}	1	3.5 and 4.8	3.6	FSBS ($n = 0$)
M_1	T_{c6}	1	3.1 and 4.8	3.04	FSBS ($n = 0$)
M_1	T_{c7}	1	3.5 and 4.4	4.3	FSBS ($n = 0$)
M_2	T_{c1}	2	4	3.1	FSK ($n = 1$) (I)
M_3	T_{c1}	1	3.5	3.4	FSK ($n = 1$) (II)
M_3	T_{c2}	1	3.5	3.2	FSK ($n = 1$) (II)
M_3	T_{c3}	1	2.6 and 4	4.22	FSK ($n = 1$) (II)
M_3	T_{c5}	3	3.1 and 4.4	4.23	FSK ($n = 1$) (II)
M_3	T_{c6}	3	3.1 and 4.4	3.44	FSK ($n = 1$) (II)
M_3	T_{c7}	2	3.1 and 4.4	3.9	FSK ($n = 1$) (II)
M_4	T_{c7}	7	3.5 and 4.8	3	SBF ($n = 2$) (I)
M_4	T_{c8}	6	3.5 and 4.4	3.17	SBF ($n = 2$) (I)
M_5	T_{c6}	8	3.5	4	SBF ($n = 2$) (II)

Notes. The first column represents the theoretical modes, which are labeled according to Figure 12. The second column shows the time interval of the subdata in which the mode was observed. In the third column, the POD mode numbers are presented as in Figure 11. The fourth column contains the frequencies (in mHz) that correspond to the peaks in the power spectrum density (PSD) of the time coefficient of the POD mode. The fifth column shows the frequency (in mHz) that corresponds to the DMD mode. Finally, the last column displays the MHD wave mode for which the POD mode and DMD mode agree well. FSBS denotes the fundamental slow-body sausage ($n = 0$) mode, FSK denotes the fast-surface kink ($n = 1$) mode, and SBF denotes the slow-body fluting ($n = 2$) mode. Here, (I) and (II) refer to two different (perpendicular) directions of the wave polarization, and n refers to the number of nodes along the azimuthal direction.

we fix the velocity perturbation to be zero at the boundary that was shown by Aldhafeeri et al. (2022) to be a valid approximation for slow-body modes in photospheric magnetic waveguides due to the very close proximity to the boundary and outermost nodes. More importantly, for interpreting slow modes inside the umbra of sunspots, it was also shown that this assumption has a negligible effect on the actual spatial structure of the modes (see Figures 2 and 3 in Aldhafeeri et al. 2022). This approximation has also been validated by observational data, which show that the Doppler velocity perturbations at the umbra/penumbra boundary for slow-body modes are indeed very small relative to the perturbations inside the umbra (see, e.g., Figures 1(c) and (d) in Stangalini et al. 2022, which show only small differences in the observation and model at the umbra/penumbra boundary).

The theoretical slow-body modes for every time interval are shown in Appendix A.1, Figures 12 and 14. The modifications in the spatial structure of the modes confirm that the higher-order modes are more sensitive to the irregularities in the cross-sectional shape shape of umbrae, i.e., the morphology of higher-order modes changes as the shape of the waveguide changes, even when these changes are small.

Next, we applied the combined POD and DMD techniques for every time interval of the HMI Doppler velocity data sets for both sunspots. The spatial structures of the first 10 POD Doppler velocity modes are shown in Appendix A.1 for each time interval. The analysis was also performed on the intensity and magnetic field data sets; however apart from the first POD modes, the higher-order modes could not be distinguished from noise. It has previously been shown that the power of intensity oscillations inside umbral regions is heavily suppressed at the photospheric level compared with the lower chromosphere (see, e.g., Nagashima et al. 2007). Here we found a similar result for the HMI intensity sunspot umbrae data, i.e., the noise level was sufficiently high to prevent extracting physical perturbations. In the HMI magnetic field data series for the sunspots analyzed in this paper the fluctuations only have a maximum amplitude of about 20 G (similar to Rubio et al. 2000), but the noise level of HMI magnetograms for a 45 s time cadence is approximately 10–15 G. Therefore, it is not surprising that physical POD modes could not be identified as was done for the Doppler velocity data where the signal-to-noise ratio was much better. We found that the maximum amplitudes for Doppler velocity were between 150 and 200 m s^{-1} compared with a noise level of 13 m s^{-1} for HMI Doppler velocity data with a 45 s time cadence.

To quantify the correlation between the POD modes obtained from every time interval of the HMI Doppler velocity data sets and the modes predicted by theoretical models, we perform a cross-correlation analysis and compute the integral of

Table 2
Summary of Possible MHD Wave Modes Observed in the Elliptical Sunspot in the Selected Time Intervals

M_i	T_{ei}	POD	Peaks of PSD (mHz)	DMD (mHz)	MHD Mode Observed
M_1	T_{e1}	7	3.6	4	FSBS ($n = 0$)
M_1	T_{e4}	3	3.6	3.4	FSBS ($n = 0$)
M_1	T_{e5}	4	3.3	3.8	FSBS ($n = 0$)
M_1	T_{e8}	8	3.3	3	FSBS ($n = 0$)
M_1	T_{e9}	8	3.6 and 4.1	3.3	FSBS ($n = 0$)
M_1	T_{e10}	5	3.3	3.4	FSBS ($n = 0$)
M_2	T_{e1}	6	3.6 and 4.1	3.3	FSBK ($n = 1$) (I)
M_2	T_{e2}	8	3.6	3.3	FSBK ($n = 1$) (I)
M_2	T_{e4}	6	3 and 3.8	3.4	FSK ($n = 1$) (I)
M_3	T_{e2}	5	3.6	3.1	FSK ($n = 1$) (II)
M_3	T_{e3}	5	3.6	3.3	FSBK ($n = 1$) (II)
M_3	T_{e5}	6	3.3 and 3.8	3.5	FSK ($n = 1$) (II)
M_3	T_{e6}	8	2.8 and 3.8	2.8	FSK ($n = 1$) (II)
M_3	T_{e9}	4	3.3	3.6	FSK ($n = 1$) (II)
M_4	T_{e1}	9	3 and 3.6	2.8	SBF ($n = 2$) (I)
M_4	T_{e7}	3	3 and 3.6	2.86	SBF ($n = 2$) (I)
M_4	T_{e8}	10	3 and 3.6	2.59	SBF ($n = 2$) (I)
M_4	T_{e10}	9	3.6	2.8	SBF ($n = 2$) (I)
M_5	T_{e3}	10	4.4	4.6	SBF ($n = 2$) (II)
M_5	T_{e9}	10	4.1	3.8	SBF ($n = 2$) (II)

Notes. The first column represents the theoretical modes, which are labeled according to Figure 14. The second column shows the time interval of the subdata in which the mode was observed. In the third column, the POD mode numbers are presented as in Figure 13. The fourth column contains the frequencies (in mHz) that correspond to the peaks in the PSD of the time coefficient of the POD mode. The fifth column shows the frequency (in mHz) that corresponds to the DMD mode. The last column displays the MHD wave mode for which the POD mode and DMD mode agree well. FSBS denotes the fundamental slow-body sausage ($n = 0$) mode, FSBK denotes the fundamental slow-body kink ($n = 1$) mode, FSK denotes the fast-surface kink mode, and SBF denotes the slow-body fluting ($n = 2$) mode. Here, (I) and (II) refer to two different (perpendicular) directions of the wave polarization, and n refers to the number of nodes along the azimuthal direction.

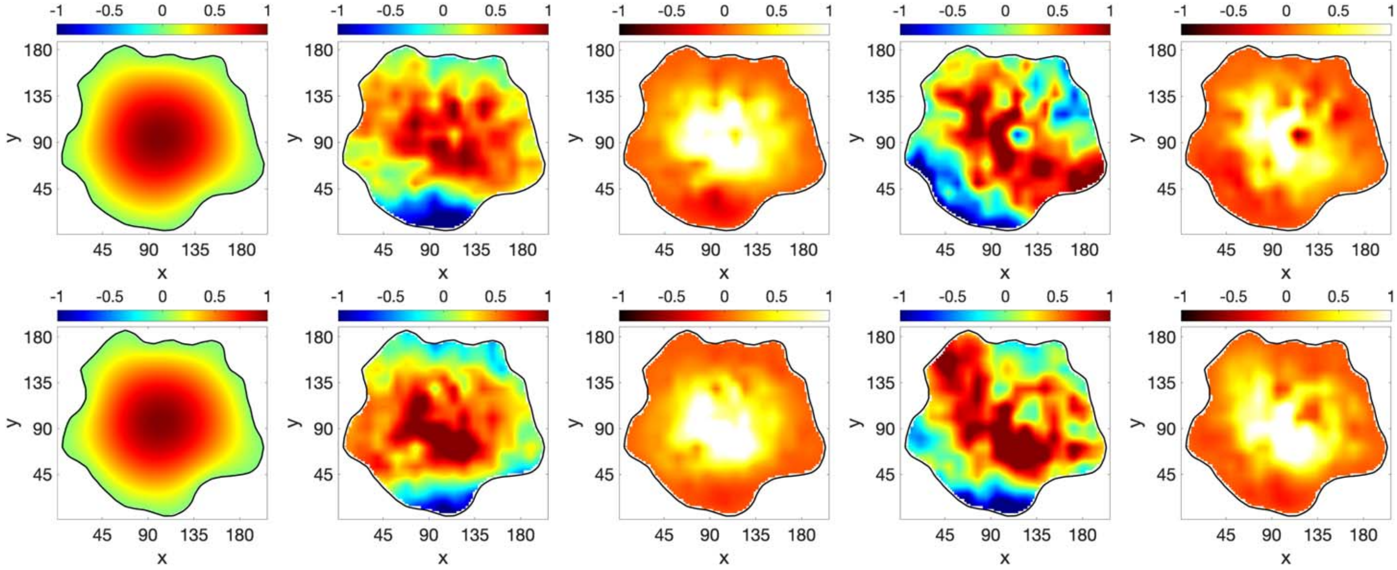

Figure 3. The results of theoretical modeling and the results of the POD and DMD analyses obtained for sunspot NOAA 11366 are presented for time intervals T_{c6} (top panel) and T_{c7} (bottom panel). The first column displays the spatial structure of the theoretically modeled fundamental slow-body sausage mode for the same shape as the umbra shape of sunspot NOAA 11366 at the particular time interval. The second column shows the spatial structure of the first (top and bottom) POD modes, where the dominant frequency of their time coefficient is in the range between 3.1 and 4.8 mHz. The cross correlation between the model and the determined POD mode is shown in the third column. The fourth column displays the spatial structure of the DMD modes that correspond to 3 mHz (top) and 4.3 mHz (bottom). Finally, the last column contains the cross correlation between the model (first column) and the DMD mode (fourth column). The solid black line shows the umbra/penumbra boundary. The same configuration was used for Figures 4 and 5. The color bars in the first column display the density perturbation obtained from the theoretical model, while the second and fourth columns display the magnitude of the Doppler velocity after being analyzed by POD and DMD, respectively. The color bars in the third and fifth columns denote the correlation/anticorrelation.

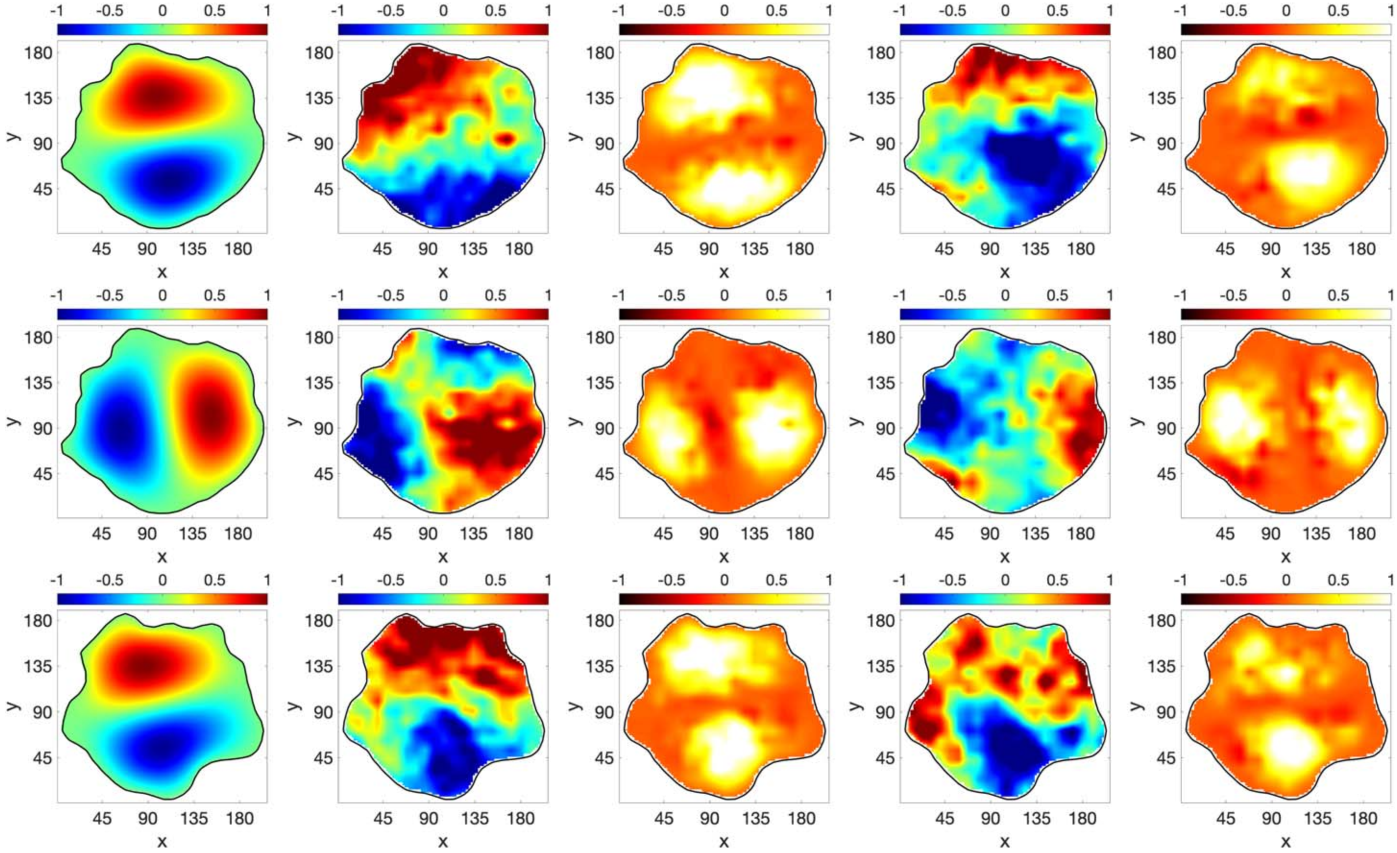

Figure 4. Same as Figure 3, but here the first row shows the first POD mode and the spatial structure of the DMD mode that corresponds to 3.4 mHz at T_{c1}. The second row shows the second POD mode and the spatial structure of the DMD mode that corresponds to 3.1 mHz at T_{c1}. The third row shows the second POD mode and the spatial structure of the DMD mode that corresponds to 3.9 mHz at T_{c7}. The first column shows the morphology of the theoretical fundamental slow-body kink mode that corresponds to T_{c1} (M_3 top panel and M_2 middle panel) and T_{c7} (M_3; bottom panel).

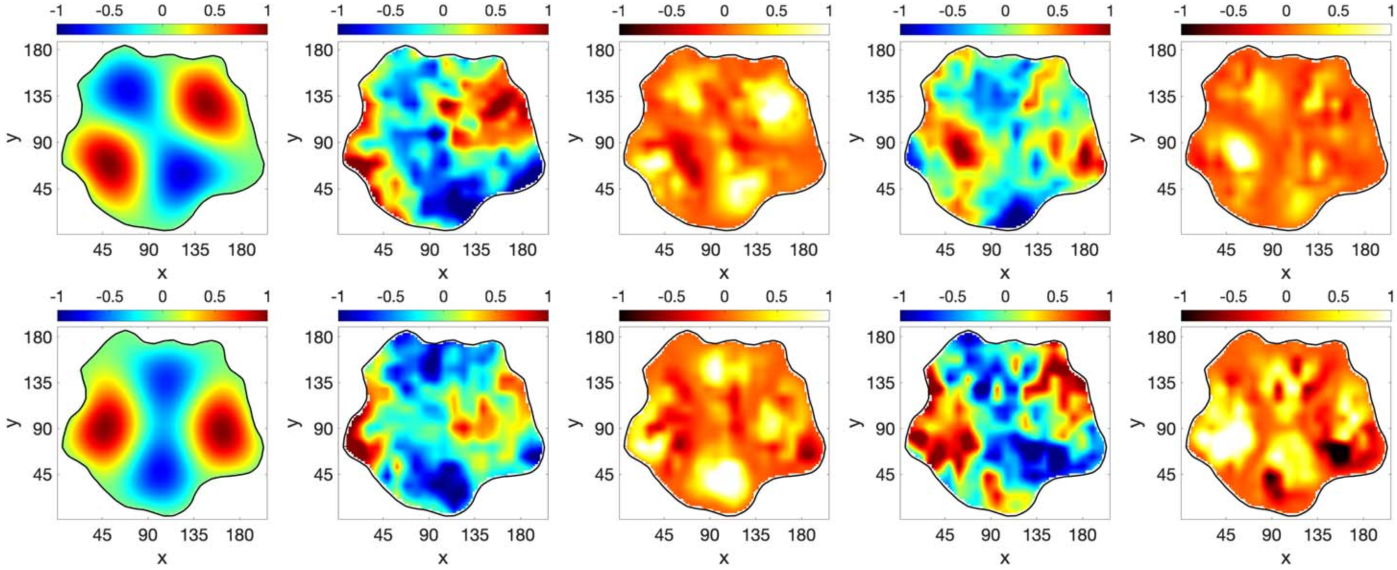

Figure 5. Same as Figure 3, but here the first row shows the eighth POD mode and the spatial structure of the DMD mode that corresponds to 4 mHz at T_6. The second row shows the seventh POD and DMD modes that correspond to 3 mHz at T_7. The first column shows the slow-body fluting ($n = 2$) that corresponds to T_6 (M_5; top panel) and T_7 (M_4; bottom panel).

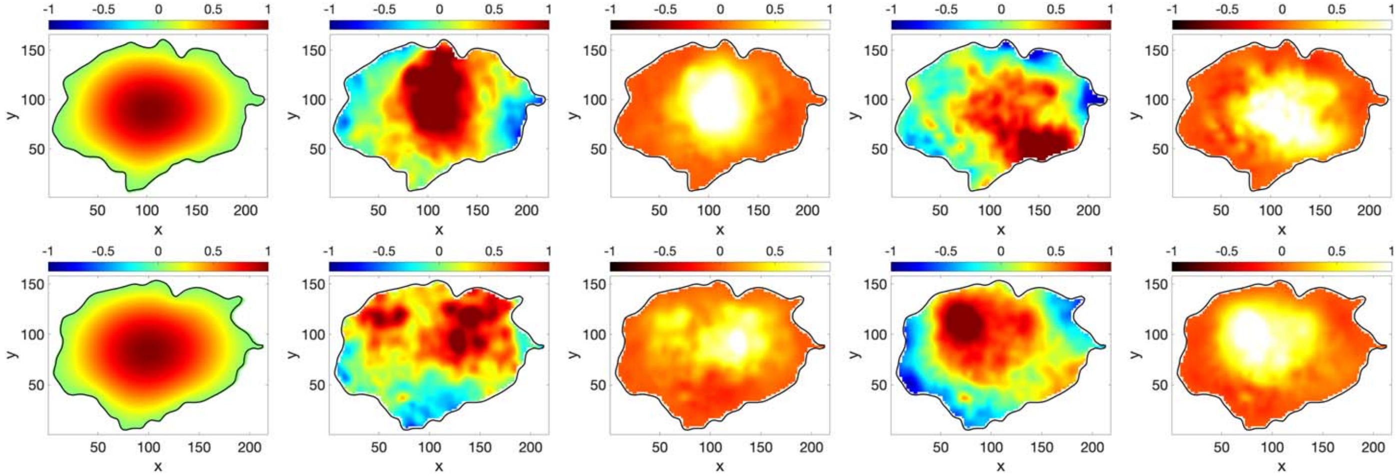

Figure 6. The results of theoretical modeling and the POD and DMD analyses obtained for sunspot NOAA 12146 are presented for the time intervals T_{e5} (top panel) and T_{e10} (bottom panel). The first column displays the spatial structure of the theoretically modeled fundamental slow-body sausage mode for the same shape as the umbra shape of sunspot NOAA 12146 at two time intervals. The second column shows the spatial structure of the fourth POD mode (top) and the fifth POD mode (bottom), where the dominant frequency of their time coefficient is in the range between 3.3 and 4 mHz. The cross correlation between the model and the determined POD mode is shown in the third column. The fourth column displays the spatial structure of the DMD modes that correspond to 3.8 mHz (top) and 3.4 mHz (bottom). Finally, the last column contains the cross correlation between the model (first column) and the DMD mode (fourth column). The solid black line shows the umbra/penumbra boundary. The same configuration was used for Figures 7 and 8.

the correlations, defined as the summation of the pixels in the correlation matrix, as shown in the Appendix A.2. This step is taken as guideline to observe and avoid missing higher correlations as we have too many modes from the POD analysis and different models for each time interval. However, these higher correlations need to be checked and validated in order to be considered. Therefore, the power spectrum of the time coefficient that corresponds to the selected POD modes is calculated to obtain the dominant frequencies. This is followed by obtaining the spatial structure of the DMD modes that correspond to the dominant frequencies.

To analyze the possible MHD modes, we selected the observed modes that presented a good agreement with the theoretical modes, i.e., those with the highest correlation. All the possible observed modes that displayed a good correlation with the theoretical models are presented in the appendices and are summarized in Tables 1 and 2, for the circular and elliptical sunspots, respectively. It is remarkable that the observed MHD modes in the elliptical sunspot have a higher-order number of POD, i.e., they have a lower contribution to the total variance along with the time intervals. In contrast, the modes observed in the circular sunspot were observed with a lower-order POD as first and second POD, which means that the observed modes have the highest contribution to the total variance of the signal.

In the case of the circular sunspot (NOAA 11366), the first MHD wave mode that was identified is the fundamental slow-body sausage mode, and it appears as the first POD mode in the time intervals from T_{c5} up to T_{c7}. This mode has a lower contribution in T_{c3} and T_{c4}, where it appears as the fourth POD mode. In Figure 3 we show the fundamental slow-body sausage

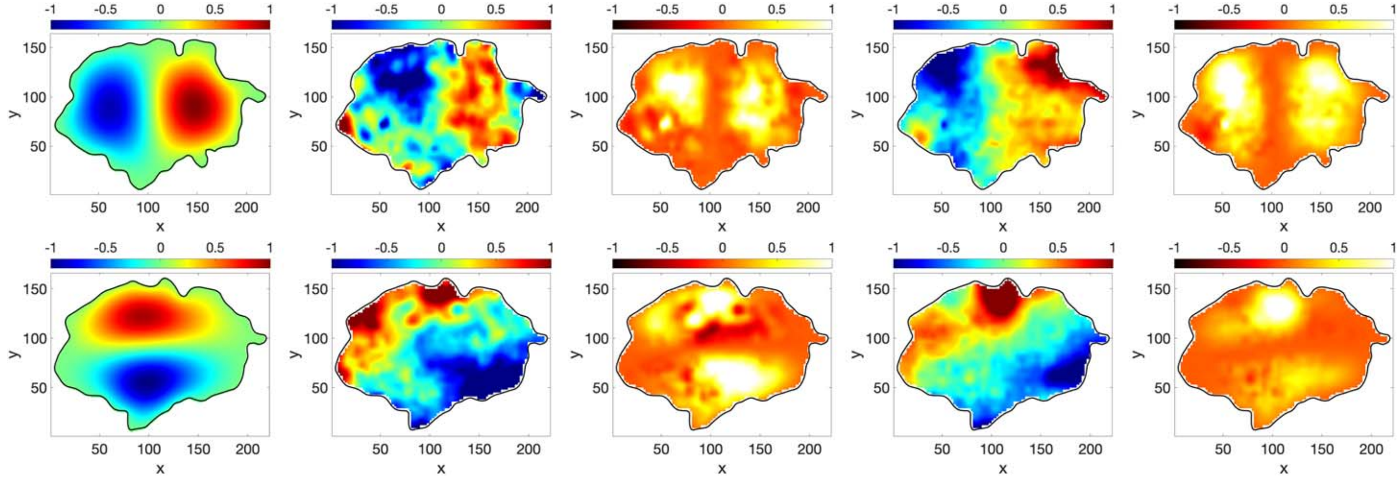

Figure 7. Same as Figure 6, but here the first row shows the sixth POD and the spatial structure of the DMD mode that corresponds to 3.3 mHz at T_{e1}. The second row shows the sixth POD and the spatial structure of the DMD mode that corresponds to 3.5 mHz at T_{e5}. The first column shows the fundamental slow-body kink mode that corresponds to T_{e1} (M_2; top panel) and T_{e5} (M_3; bottom panel).

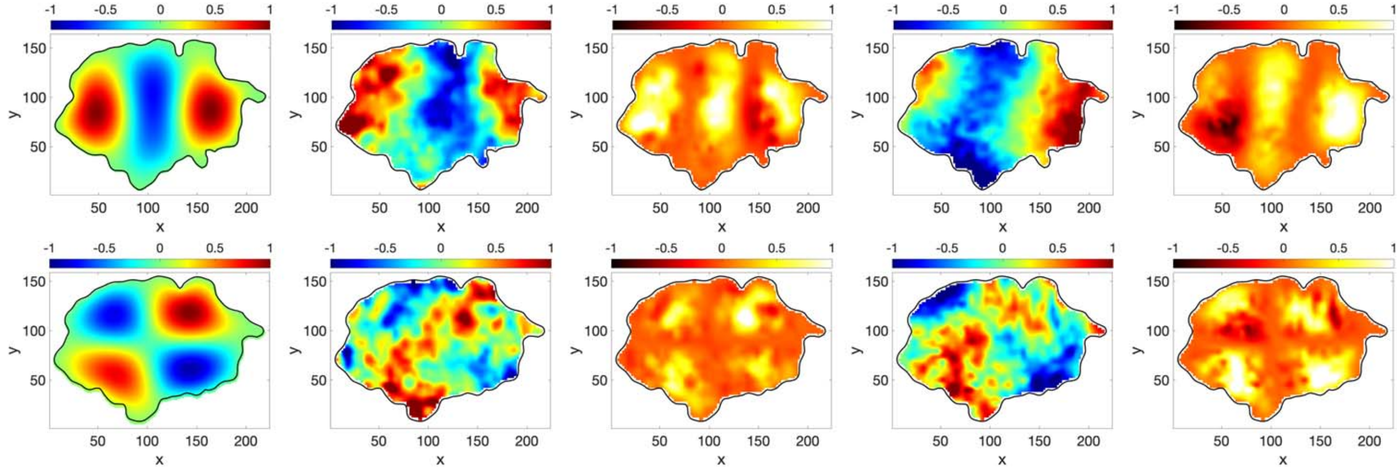

Figure 8. Same as Figure 6, but here the first row shows the ninth POD and the spatial structure of DMD mode that corresponds to 2.8 mHz at T_{e1}. The second row shows the ninth POD and the spatial structure of DMD mode that corresponds to 4.6 mHz at T_{e3}. The first column shows the slow-body fluting ($n = 2$) mode that corresponds to T_{e1} (M_4; top panel) and T_{e3} (M_5; bottom panel).

mode in two time intervals (T_{c6} and T_{c7}, corresponding to the two rows) and the spatial structure of the DMD mode that corresponds to the dominant frequency of the time coefficient of the POD modes, which are in the range between 3.1 and 4.8 mHz. These DMD modes correspond to 3 mHz in T_{c6} and 4.3 mHz in T_{c7}. The determined POD and DMD modes are compared with the theoretical model by applying the cross-correlation analysis, and they show good agreement.

The second MHD mode that we observed has an azimuthal asymmetry that corresponds to the fast-surface kink mode, and it is shown in Figure 4. The patterns of these modes correspond to surface waves; as the amplitude increases along the radial direction, they attain their maximums at the boundary. Due to the limitations of the theoretical model that is used to describe waves in a waveguide, the only modes that can be determined are the slow-body modes. Hence, the cross correlation with possible surface modes detected by means of POD/DMD and their direct theoretical counterparts cannot be performed. However, as it was shown in the study by Albidah et al. (2022), the cross correlation between the slow-body mode and the fast-surface mode provides a spatial structure with a pattern closed to that of the slow-body mode. In contrast, the cross correlation between the slow-body mode and the slow-surface mode produces a spatial structure similar to a ring for the sausage mode and to a broken ring for the kink mode.

Therefore, the correlation in Figure 4 between the slow-body modes and the observed modes shows a pattern similar to that of the slow-body mode; hence we can identify this mode as being a fast-surface kink. The modes that are presented in the first and second rows of the second and fourth columns of Figure 4 are the first and second POD modes and the DMD modes that corresponds to 3.4 and 3.1 mHz, respectively, at T_{c1}. The superposition of these two approximately perpendicular kink modes with close frequencies can provide an apparent rotational motion. The mode presented in the third row of Figure 4 is the second POD and DMD modes that corresponds to 3.9 mHz at T_{c7}. The dominant frequencies of the POD modes that have an azimuthal symmetry to the kink mode are in the range between 3 and 4 mHz.

The fast-surface kink mode is still present in the remaining time intervals, but with a lower contribution as this mode becomes the third POD mode at T_{c5} and T_{c6} and the second POD at T_{c7}. The last MHD wave mode that we have observed in the circular sunspot is the slow-body fluting mode ($n = 2$), which appears at T_{c6} and T_{c7} (see Figure 5). The first row of Figure 5 shows the eighth POD and

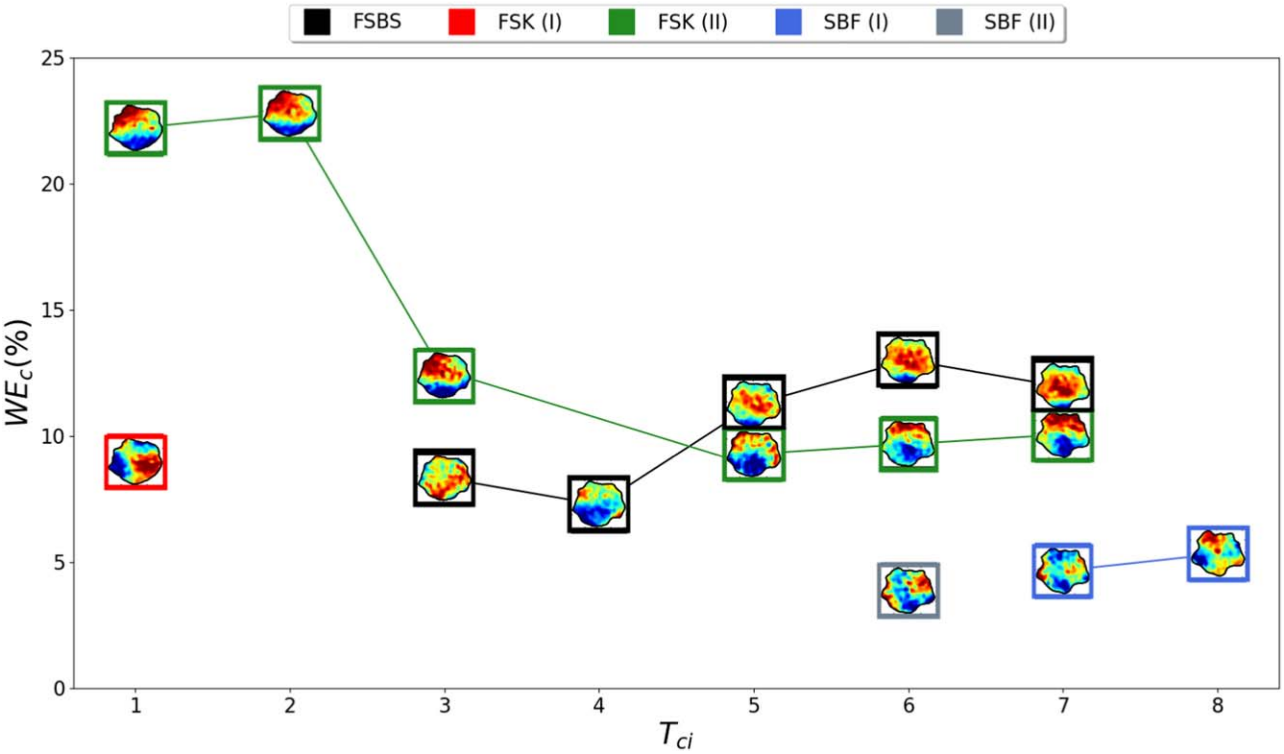

Figure 9. Wave contribution from the observed MHD modes to the total variance of the signal in the case of the circular sunspot, WE_c, as a function of time. The values of WE_c correspond to the contribution of the POD mode linked to MHD wave mode in each time interval, T_{ci}. Different modes are shown by different colors, as indicated by the legend in the upper part of the plot. Here, FSBS stands for the fundamental slow-body sausage ($n = 0$) mode, FSK for the fast-surface kink ($n = 1$) mode, and SBF for the slow-body fluting ($n = 2$) mode, while (I) and (II) refer to two different (perpendicular) directions of the wave polarization.

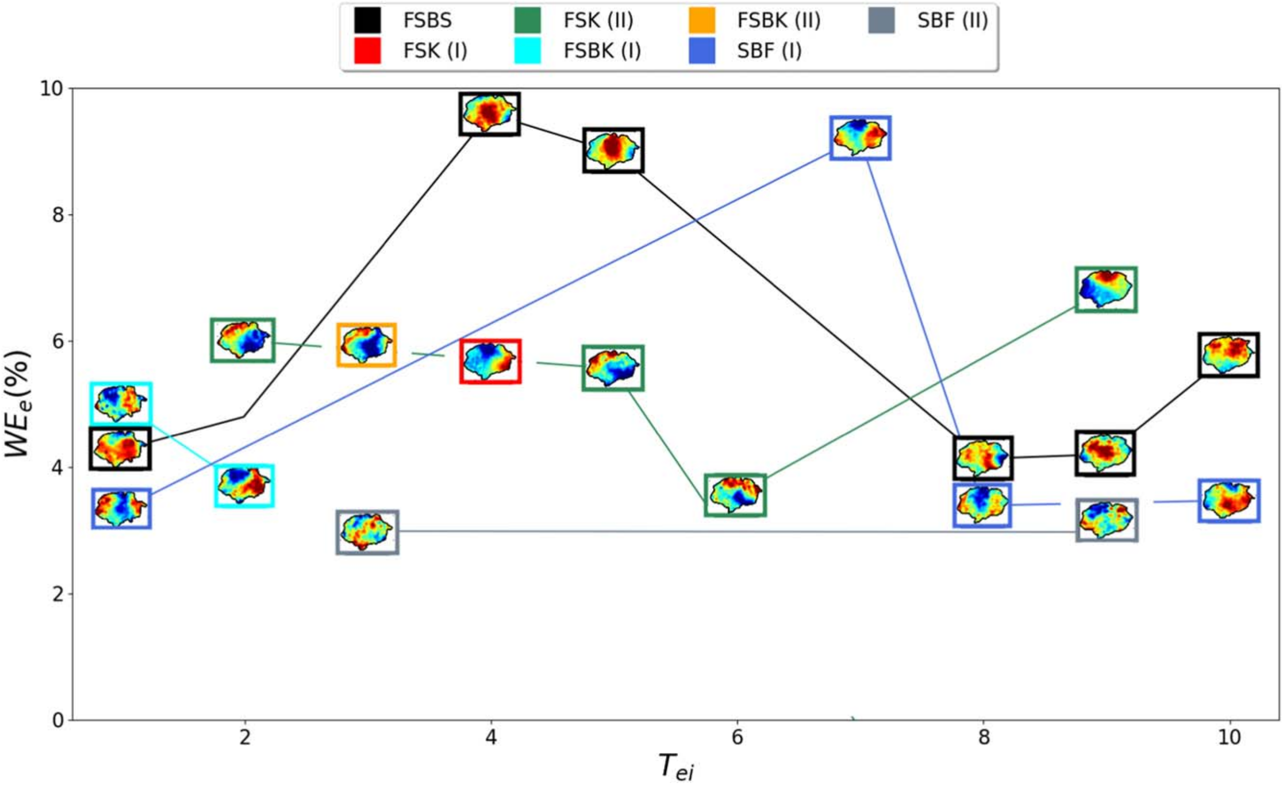

Figure 10. Wave contribution from the observed MHD wave modes to the total variance of the signal for the elliptical sunspot, WE_e, as a function of time. The values of WE_e correspond to the contribution of the POD mode linked to MHD wave mode at each time interval, T_{ei}. The identified MHD modes are shown by different colors and specified by the legend in the upper part of the plot. The abbreviation of possible modes is identical with the one used in Figure 9.

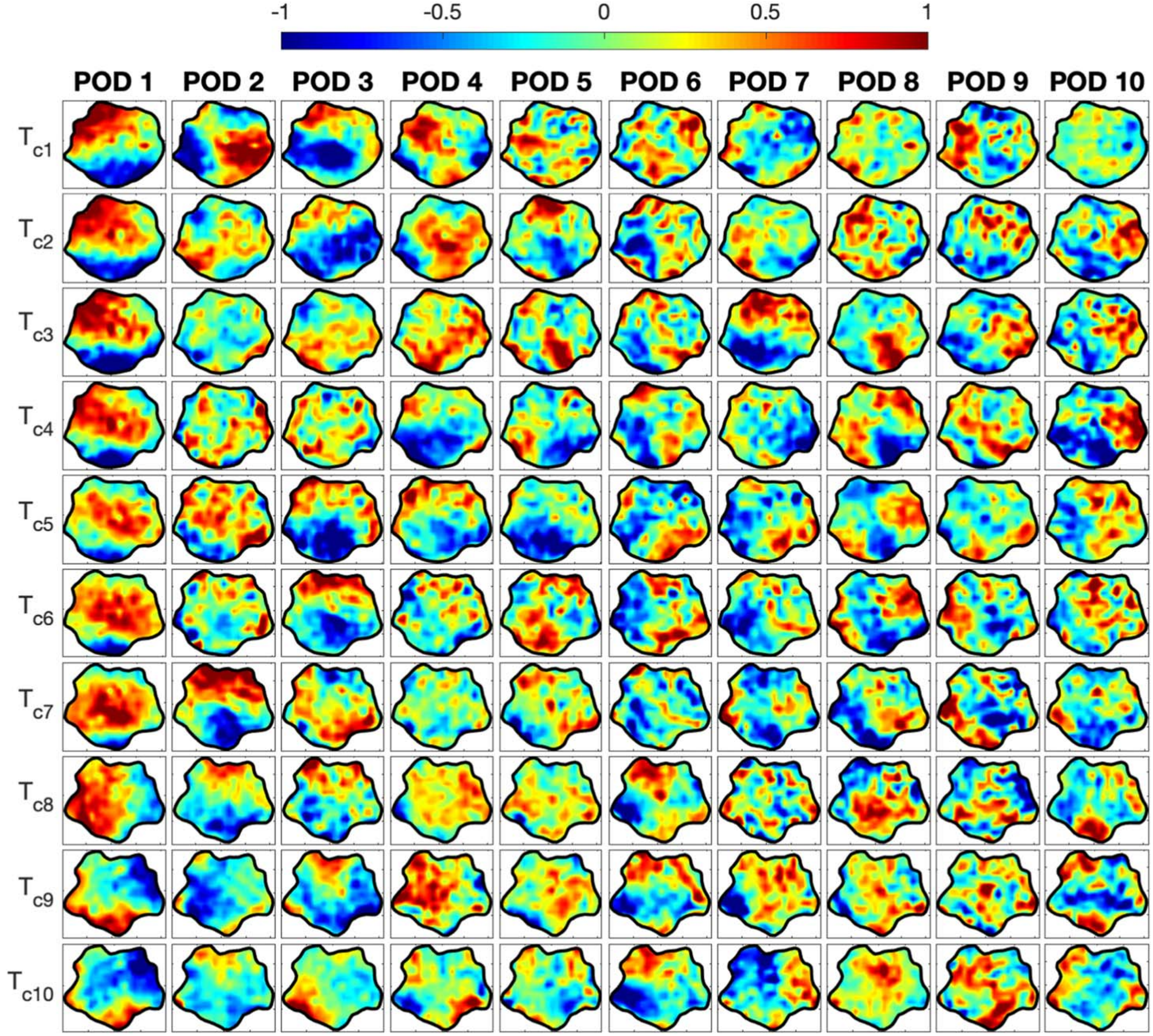

Figure 11. First 10 POD modes of the circular sunspot. Every column shows a POD mode, and the rows show how the modes change at each time interval, T_{ci}, of the data time series. Every time interval contains 50 images and has a duration of 37.5 minutes. Every time interval is shifted by 20 images, i.e., the initial time of T_{ci+1} is after the initial time of T_{ci} by 20 images, which corresponds to 15 minutes.

DMD modes that correspond to 4 mHz at T_{c6}. The second row of this figure shows the seventh POD and DMD modes that correspond to a frequency of 3 mHz at T_{c7}.

For the elliptical sunspot, the first 10 POD modes and the models, at every time interval, are shown in Appendix A.1. The POD modes that show a good agreement with the theoretical predictions are presented in Table 2. In Figures 6–8, we display examples of the observed modes obtained through the POD and DMD analyses at different time intervals, providing the cross-correlation analysis with the theoretical mode that corresponds to the realistic shape of the sunspot. The first MHD mode is the fundamental slow-body sausage mode, which is observed in most time intervals, as shown in Table 2. Figure 6 shows the fundamental slow-body sausage mode at T_{e5} and T_{e10}. The first row of Figure 6 shows the spatial structure of the fourth POD mode and the DMD mode that corresponds to 3.8 mHz at T_{e5}, while the second row shows the spatial structure of the fifth POD mode and the DMD mode that corresponds to 3.4 mHz at T_{e10}. The dominant frequency of the time coefficient of the POD modes is in the range of 3.3–4 mHz.

The second MHD mode that we have identified is the fundamental slow-body kink mode, as shown in first row of Figure 7. The first row of Figure 7 shows the sixth POD mode and the DMD mode that correspond to 3.3 mHz at T_{e1}, which has an azimuthal symmetry that corresponds to the slow-body kink mode. The second row displays the sixth POD mode and the DMD mode that correspond to 3.5 mHz at T_{e5}. As the amplitude of the observed modes in the second row of Figure 7 increases as we approach the edge of the umbra and as the cross correlation between the observed modes and the theoretical model gives a pattern closed to the slow-body mode, the mode shown in the second row of Figure 7 is identified as the fast-surface kink mode.

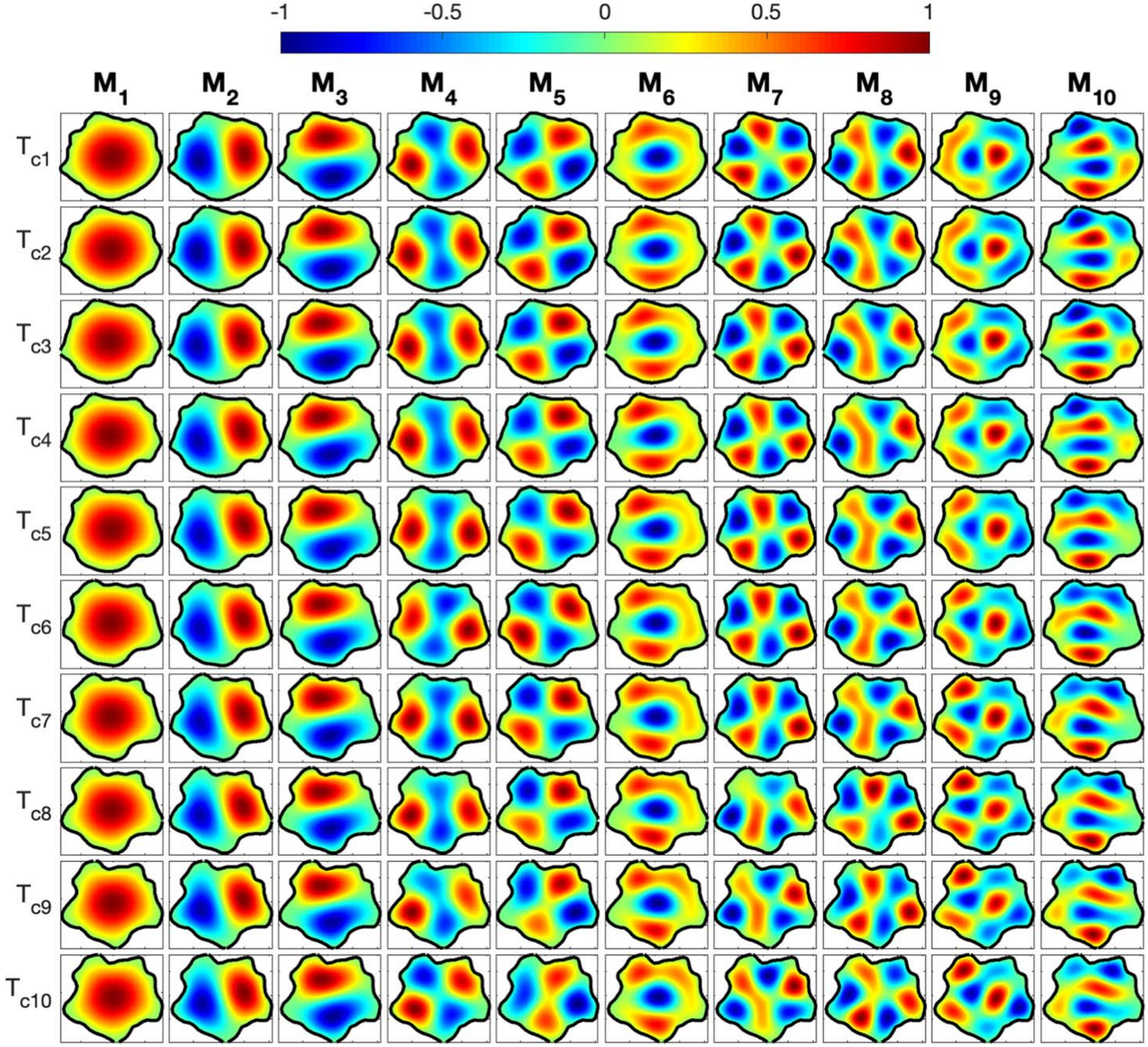

Figure 12. Theoretical eigenfunctions that correspond to the changing shapes of the observed circular sunspot (see Figure 11). Every row shows the spatial structure of the models at different times and the changing shape. The columns represent different types of slow-body modes, and they are labeled by M_i, where $i = 1,...,10$. In particular, M_1 is for fundamental sausage ($n = 0$), M_2 and M_3 are for fundamental kink ($n = 1$), M_4 and M_5 are for fluting ($n = 2$), M_6 is for sausage overtone ($n = 0$), M_7 and M_8 are for fluting ($n = 3$), and the last two columns (M_9 and M_{10}) are for kink overtone ($n = 1$).

The last MHD mode that we have identified in the elliptical sunspot is the slow-body fluting ($n = 2$) mode, as shown in Figure 8. The first row of Figure 8 shows the ninth POD mode and the DMD mode that corresponds to 2.8 mHz at T_{e1}, while the second row shows the tenth POD mode and the DMD mode that corresponds to 4.6 mHz at T_{e3}. It is evident that the morphology of this wave considerably changes in time as the shape of the waveguide changes.

The POD decomposes the modes and provides their ranking according to their contribution to the overall energy of the signal (Albidah et al. 2021, 2022). The time evolution of the wave energy (WE) contribution is calculated for the case of a circular sunspot (WE$_c$) and an elliptical sunspot (WE$_e$). The observed WE of POD modes, which were identified as MHD wave modes, i.e., the modes with the highest correlation value between theoretical and observed counterparts, are shown in Figures 9 and 10. The time-dependent behavior of WE$_c$ and WE$_e$ is similar and, as expected, the main contribution to the wave energy is provided by fundamental modes. For the case of the circular sunspot (Figure 9), the fast-surface kink mode has the dominant contribution initially but then the fundamental slow-body sausage mode appears with higher contribution starting from time interval T_{c5}. The slow-body fluting ($n = 2$) mode has, approximately, a 2 times smaller contribution. This change in behavior could be related to the change in the wave driver from being azimuthally antisymmetric to symmetric. The higher-order wave modes in this case are less frequently excited.

In the case of the elliptical sunspot illustrated in Figure 10, the fundamental slow-body sausage and fast-surface kink modes have an antiphase behavior in time compared with the circular sunspot with regards to growth and decay in contribution. In contrast to the previous case, the higher-order modes, i.e., slow-body fluting ($n = 2$) modes (with two different polarizations) are notably present. The contribution to the signal's energy attributed to these modes grows steadily in time, followed by a sudden decay. The body and surface kink ($n = 1$) modes were observed with different polarization of the wave along the major and minor axes. Additionally, the kink mode was observed with an accidental appearance of their contribution along the time intervals, as shown in Figure 10.

4. Summary and Conclusions

In the present study, we have focused on the changes in the spatial structure of umbral slow-body modes by accounting for the dynamical change in time of the shapes of the umbral boundaries of two sunspots. We employed the same theoretical model used successfully by Stangalini et al. (2022), who showed that that the perturbations in the line-of-sight velocity component decay very rapidly at the umbra/penumbra boundary. Every acoustic or MHD wave model requires a boundary condition to solve the governing equations. For *p*-mode models the Lagrangian pressure perturbation is taken to be exactly zero at the Sun's surface. There are uncertainties in both the size of the pressure perturbation and the exact location of the Sun's "surface". However, the approximation has worked well. The benefits outweigh the drawbacks. With the standard Edwin & Roberts (1983) cylinder model the background quantities have a tangential discontinuity at the flux tube boundary. Again, this is an approximation of reality, but it is needed to derive dispersion relations. It was shown by Aldhafeeri et al. (2022) that the outer slow-body mode node and boundary are very close together in space, which justifies our approximation. For our theoretical model, the employed boundary condition has the vast benefit that we can use the exact irregular observed umbral shape to model slow-body mode eigenfunctions. This is the main goal of the paper, i.e., to investigate how the changing shape of sunspot umbrae affects the spatial structure of the slow-body modes. The standard cylinder model is simply not applicable to study the evolution of umbral slow-body modes identified by our analysis because the model prescribes that the cross-sectional shape of the waveguide is always fixed as a perfect circle.

The POD and DMD techniques used here are the same as ones presented earlier (e.g., Albidah et al. 2021, 2022); however, in these studies the shapes of the umbrae were considered to be stationary. Each analyzed Doppler velocity data set was divided equally into 10 overlapping time intervals. and then POD and DMD were applied separately to the data sets within each time interval. The identified modes were cross-correlated with the theoretically obtained counterparts, which were determined by taking the same shape of the umbra within selected time intervals. The comparison was calculated on a pixel-by-pixel basis of the cross-correlation analysis. It was shown that even minor changes in the shape of umbrae alter the morphology and nature of wave modes, in particular higher-order modes.

We found that the main contribution to the overall energy of the signal is provided by fundamental modes and the energy contribution from waves may considerably change in time. Given the far-from-ideal spatial and temporal resolution of the HMI instrument, it is likely that some significant information on the dynamics within the sunspots cannot be acquired or resolved. As a result, there could be other higher-order modes or further overtones that cannot be identified in our analysis. Nevertheless, POD/DMD have shown their ability to identify higher-order modes and overtones for observations that have a much better spatial and temporal resolution, e.g., the Hα time series (Albidah et al. 2022). From the performed analysis it follows that the optimal time length needed to assess the impact of changes in the umbral shape on observed wave modes was 37 minutes for the circular sunspot and 60 minutes for the elliptical sunspot. This estimate, however, may depend on the spatiotemporal resolution of the sunspot data.

Our results show that the fundamental modes are less sensitive to changes in the sunspot shape. We conclude that wave modes variations within umbral regions may be related to changes in the nature of the driver. For higher modes, proper detection needs to consider the variation in umbral shape as their theoretical eigenfunctions present higher variability in time, affecting the identification of the POD mode and thereby their contribution to the energy of the signal. We found that the analysis of the data using optimal time intervals is essential to capture the dynamical contribution of each mode to the observed signal, allowing use to find significant statistics on the temporal evolution of wave modes in future analyses. Moreover, a spectral principal-component analysis based on a sequence of time intervals may allow for the correlation between the observed wave mode dynamics and the nature of the wave driver.

Acknowledgments

A.B.A. would like to thank Deanship of Scientific Research at Majmaah University for supporting this work under Project No. (ICR-2023-464). V.F., G.V., and I.B. are grateful to the Royal Society, International Exchanges Schemes, collaborations with Pontificia Universidad Catolica de Chile, Chile (IES/R1/170301), Aeronautics Institute of Technology, Brazil, (IES/R1/191114), Monash University, Australia (IES/R3/213012) and Instituto de Astrofisica de Canarias, Spain (IES/R2/212183). V.F. and S.S.A.S. are grateful to the Science and Technology Facilities Council (STFC), grant ST/V000977/1. This research has also received financial support from the ISEE, International Joint Research Program (Nagoya University, Japan) and the European Union's Horizon 2020 research and innovation program under grant agreement No. 824135 (SOLARNET). A.A.A. acknowledges the Deanship of Scientific Research (DSR), King Faisal University, Al-Hassa (KSA), for financial support under grant Track (grant No. 1267). D.B.J. acknowledges support from the UK Space Agency for a National Space Technology Programme (NSTP) Technology for Space Science award (SSc 009) and The Leverhulme Trust for grant RPG-2019-371. D.B.J. also wishes to thank STFC for additional funding via the grant awards ST/T00021X/1 and ST/X000923/1. Finally, V.F., G.F., D.B.J., and M.S. wish to acknowledge scientific discussions with the Waves in the Lower Solar Atmosphere (WaLSA; www.WaLSA.team) team, which has been supported by the Research Council of Norway (project No. 262622), The Royal Society (award No. Hooke18b/SCTM), and the International Space Science Institute (ISSI Team 502). We are also very grateful to Mr. Miguel S. A. Schiavo for his patience and encouragement.

Appendix

A.1. POD and Model Time Interval

The spatial structure of the first 10 POD modes of the circular sunspot at every time interval T_{ci} and the MHD modes

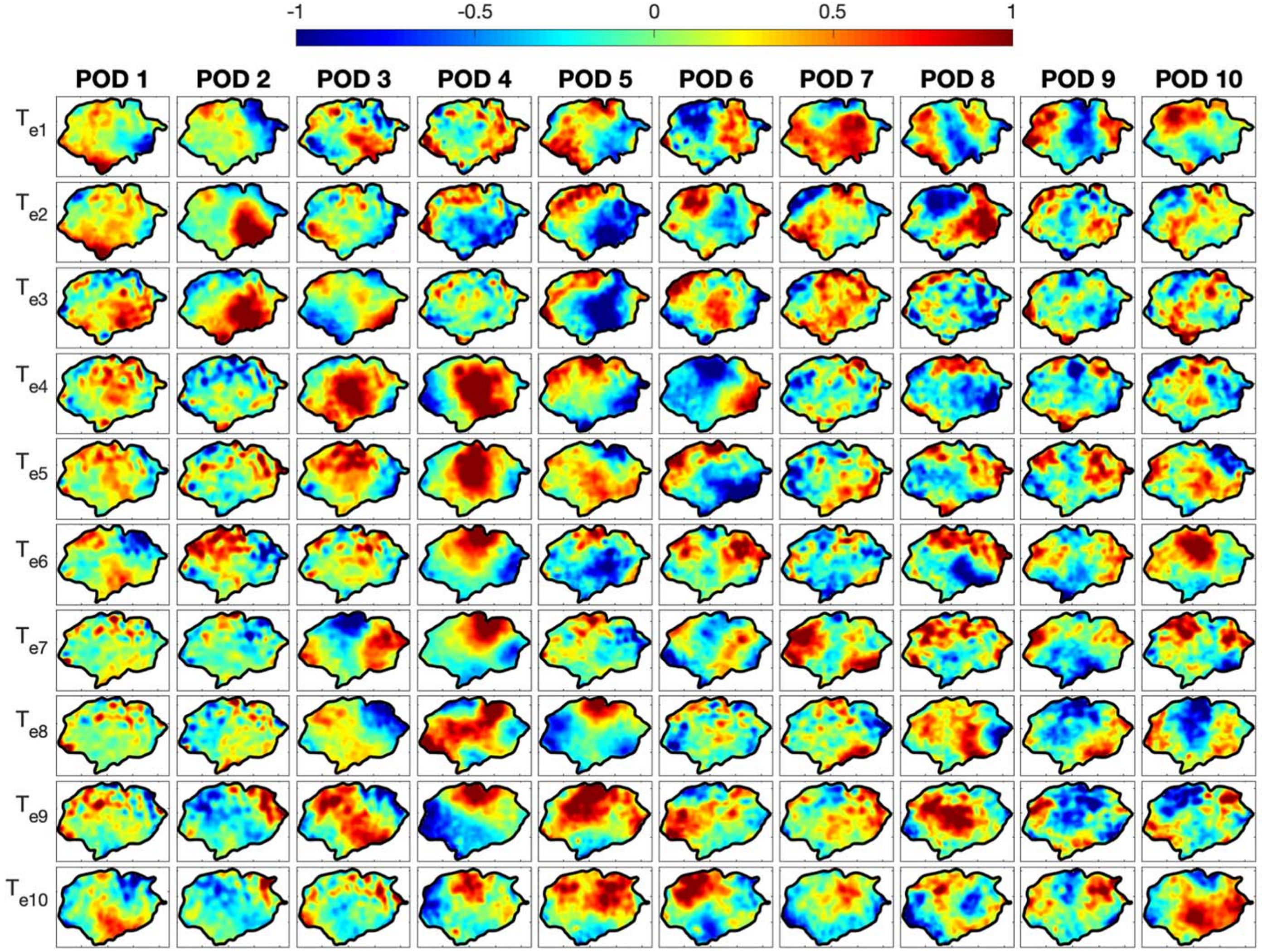

Figure 13. First 10 POD modes of the elliptical sunspot. Every column shows a POD mode, and the rows show how the modes change at each time interval, T_{ei}, of the data time series. Every time interval contains 80 images and has a duration of 60 minutes. Every time interval is shifted by 40 images, i.e., the initial time of T_{ei+1} is after the initial time of T_{ei} by 40 images, which correponds to 30 minutes.

that correspond to the exact shape of the umbra are shown in Figures 11 and 12, respectively. Similarly, Figures 13 and 14, show the spatial structure of the first 10 POD modes at every time interval T_{ei} and MHD modes that correspond to the exact shape of the umbra of the elliptical sunspot, respectively.

A.2. Correlation

The cross correlation between the observed and the theoretical modes has been calculated on a pixel-by-pixel basis for all time intervals. For every correlation matrix, we have taken the summation of the pixels, and hence for every single correlation of the observed and the theoretical mode is represented as an integer. As a result, we have obtained the correlation panels shown in Figures 15 and 16 for the circular and elliptical sunspots, respectively. Every panel refers to a different time interval. For example, the upper left panel of Figure 15, labeled T_{c1}, refers to the correlation of the POD modes in the first row of Figure 11 and theoretical modes in the first row of Figure 12.

At the end, every column of the correlation panels are normalized by the maximum value of that column along all time intervals. This step is required to make the correlation of higher-order modes visible. Without this step, the correlation of the sausage and kink modes will be the dominant and other modes will not be visible as high correlation. However, the higher correlations need to be checked and validated in order to be considered.

A.3. Further Time Intervals of POD Analysis

Our analysis was also applied on different time intervals than those presented in Figures 11 and 13. This step was applied to ensure that the widths of the time intervals (37.5 minutes for the circular sunspot and 60 minutes for the elliptical sunspot) are working well and that the results are robust. It is important to mention that, all time intervals (T_{ci} and T_{ei}) that are mentioned in the text above, Tables 1–2 and Figures 2–8 refer to thise in Figures 11 and 13 for the circular and elliptical sunspots, respectively.

For the circular sunspot, we have decreased the period of the time interval to 22.5 minutes with an overlapping time of 11 minutes. The results of the POD analysis of the time intervals are shown in Figure 17, and the theoretical models that correspond to the shape are shown in Figure 18. In addition, we have increased the period of the intervals to 60 minutes with an overlapping time of 30 minutes. The spatial structure of the

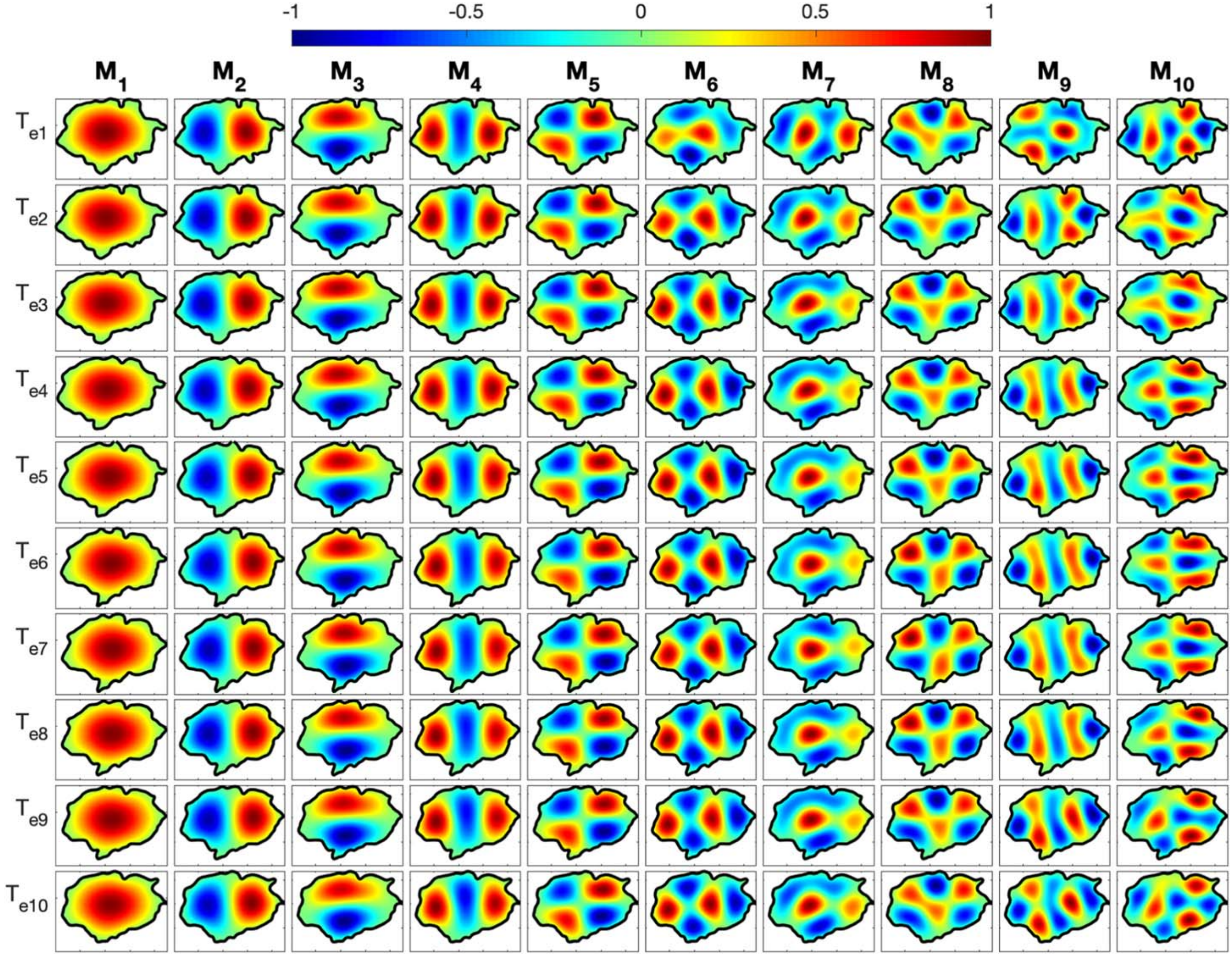

Figure 14. Theoretical eigenfunctions that correspond to the changing shapes of the observed elliptical sunspot (see Figure 13). Every row shows the spatial structure of the models at different times and the changing shape. The columns represent different types of slow-body modes, and they are labeled by M_i, where $i = 1,...,10$. In particular, M_1 is for fundamental sausage ($n = 0$), M_2 and M_3 are for fundamental kink ($n = 1$), M_4 and M_5 are for the fluting ($n = 2$), M_6 is for sausage overtone ($n = 0$), M_7 and M_8 are for the fluting ($n = 3$), and the last two columns (M_9 and M_{10}) are for kink overtone ($n = 1$).

POD analysis is shown in Figure 19, and the theoretical models that correspond to the actual shape are shown in Figure 20.

Similarly, for the elliptical sunspot, we have decreased the period of the time intervals to be 37.5 minutes, with an overlapping time of 22.5 minutes. The results of the POD and the theoretical models are shown in Figures 21 and 22, respectively. We have also increased the period of the time intervals to be 75 minutes, with an overlapping time of 37.5 minutes, and the result of the POD and the theoretical models are shown in Figures 23 and 24, respectively. A different time sequencing, obviously, will modify the complexity of the recovered signal; however, the patterns we obtained in the case of our investigation still persist. Shorter time sequences used for POD/DMD analysis provide more precise information on mode changes and their individual contributions to the signal identified in the larger time sequence. For example, this is clearly visible in the first columns of Figures 13 and 21 for the time intervals $T_{e1} - T_{e3}$ and $T_1 - T_6$, respectively.

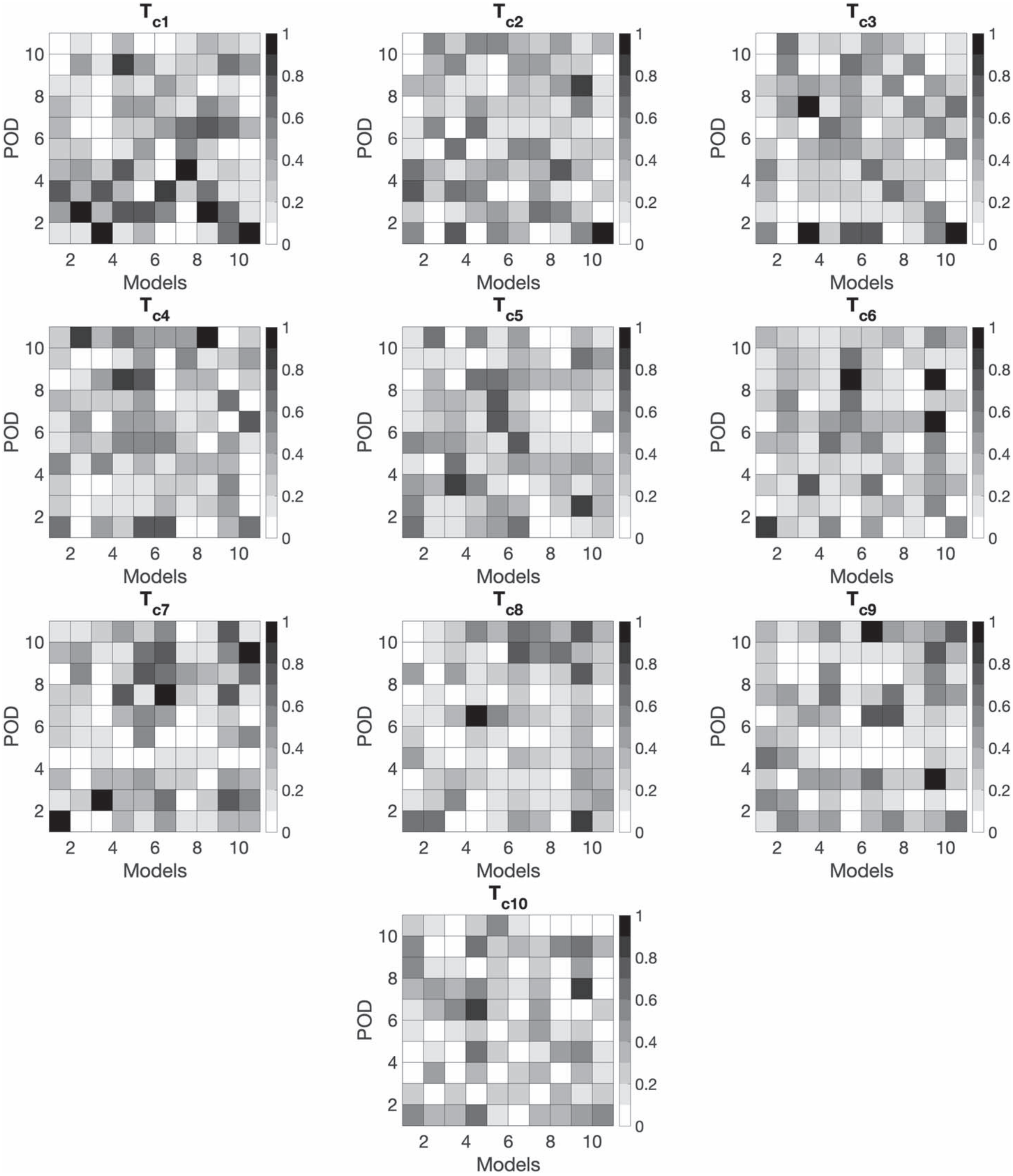

Figure 15. Summation of pixels in the correlation matrix between the POD modes in Figure 11 and the theoretical models in Figure 12, for every T_{ci}. The color bar shows the amplitude of the summation of the correlation matrix. The maximum value of each column was normalized along all time intervals.

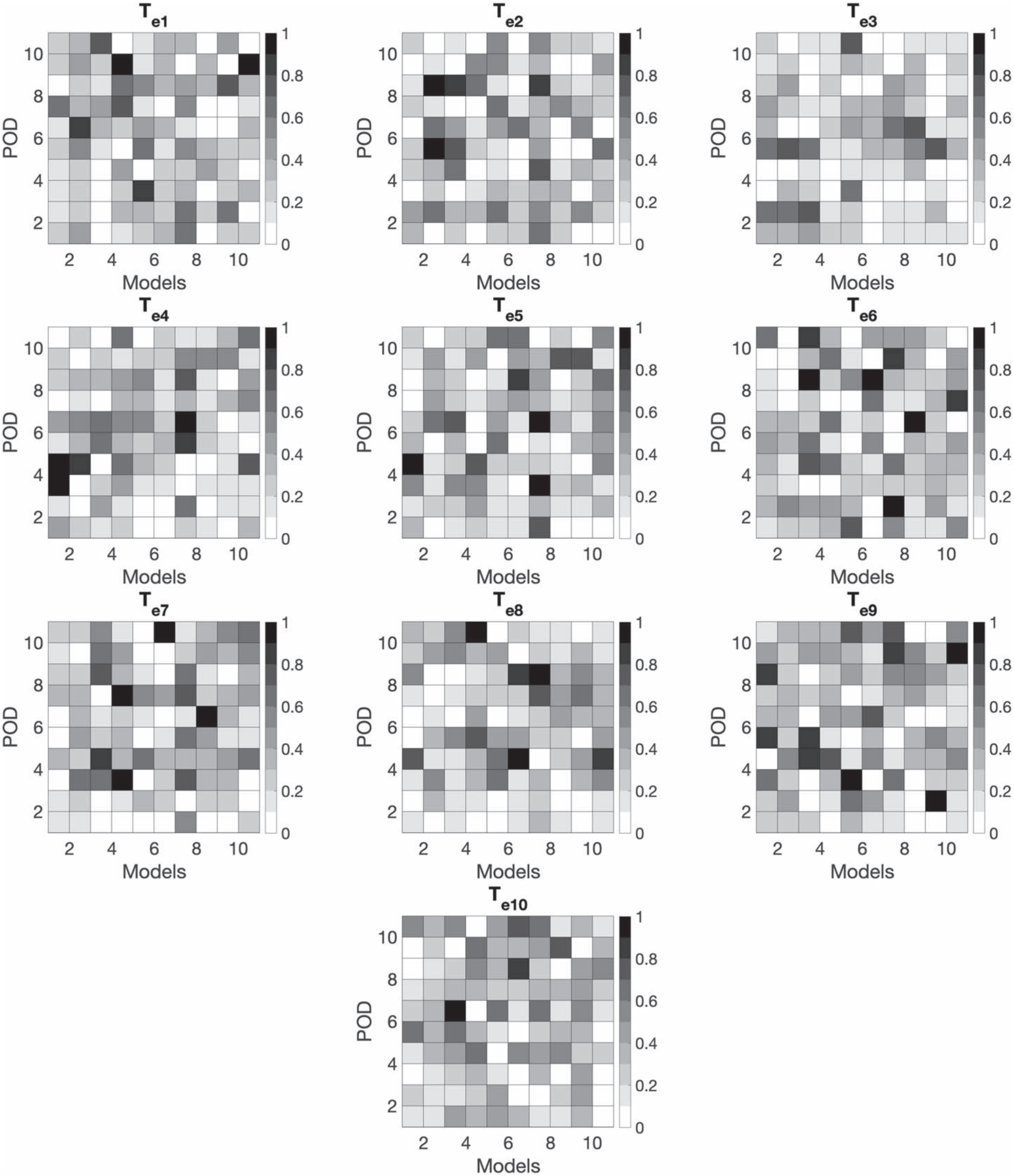

Figure 16. Summation of pixels in the correlation matrix between the POD modes in Figure 13 and the theoretical models in Figure 14, for every T_{ei}. The color bar shows the amplitude of the summation of the correlation matrix. The maximum value of each column was normalized along all time intervals.

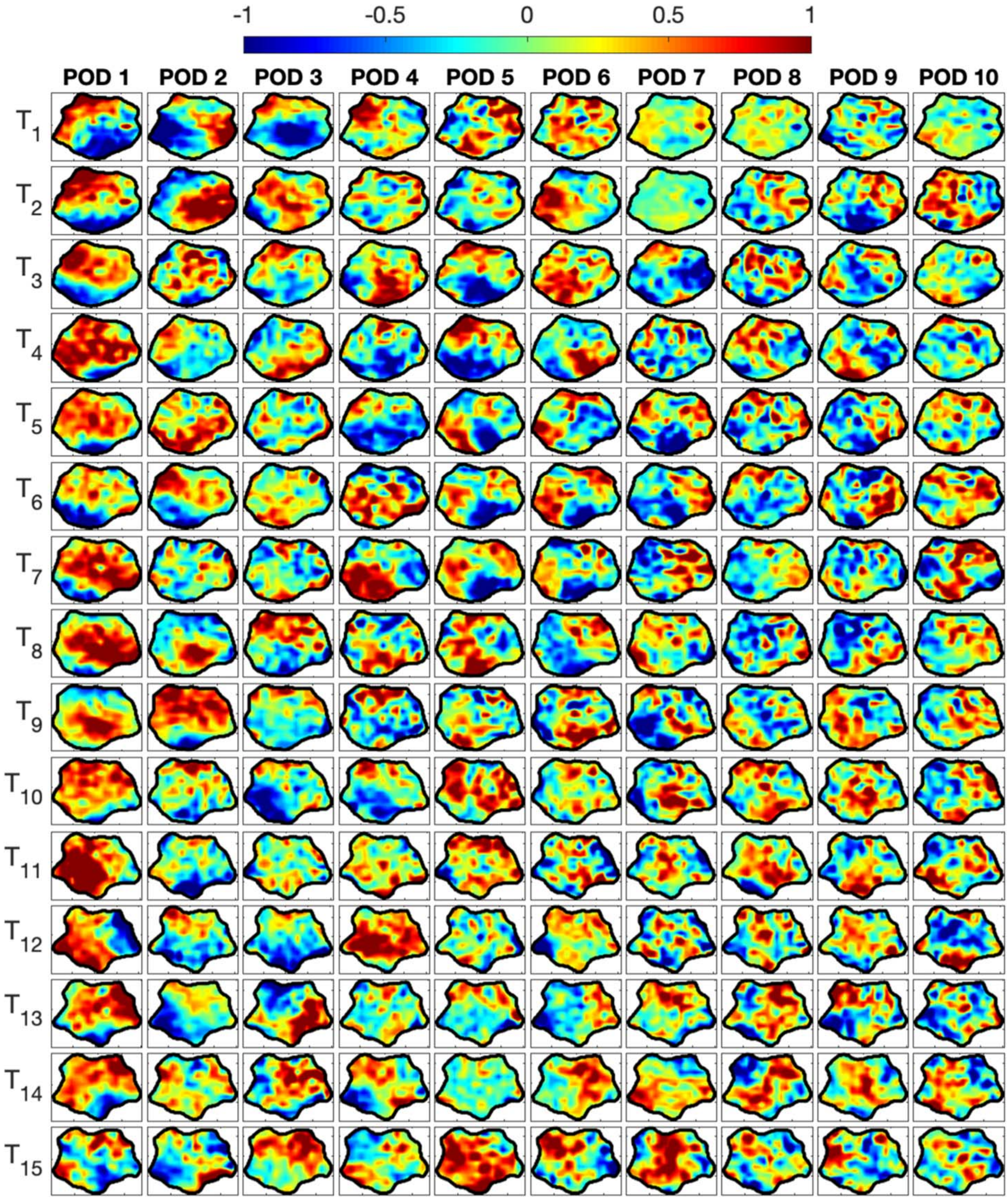

Figure 17. First 10 POD modes of the circular sunspot. Every column shows a POD mode, and the rows show how the modes change at each time interval, T_i, of the data time series. Every time interval contains 30 images and has a duration of 22.5 minutes. Every time interval is shifted by 15 images, which correponds to 11 minutes.

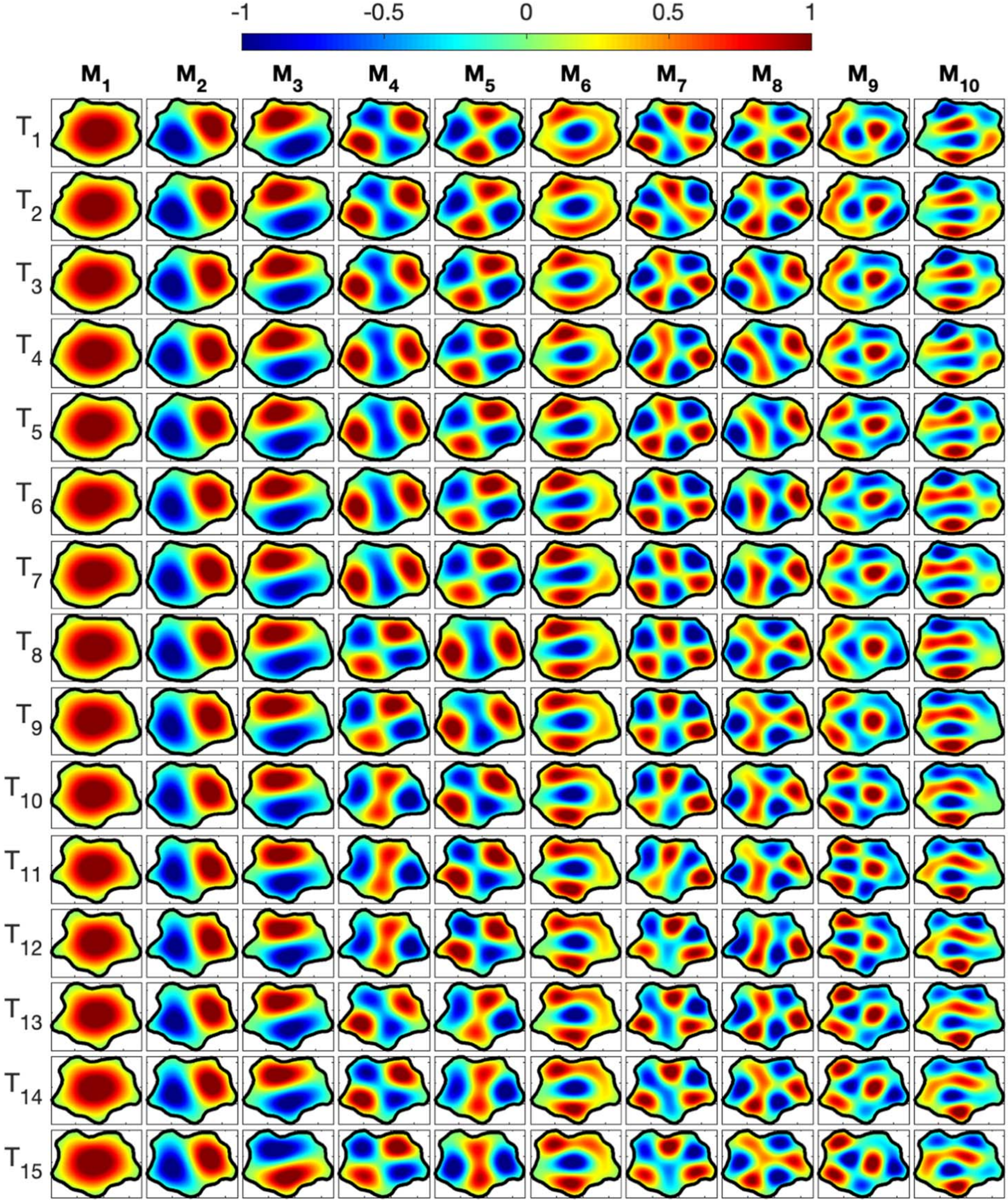

Figure 18. Theoretical eigenfunctions that correspond to the changing shapes of the observed circular sunspot (see Figure 17). Every row shows the spatial structure of the models at different times and the changing shape. The columns represent different types of slow-body modes, and they are labeled by M_i, where $i = 1,...,10$. In particular, M_1 is for the fundamental sausage, M_2 and M_3 are for fundamental kink, M_4 and M_5 are for fluting ($n = 2$), M_6 is for sausage overtone, M_7 and M_8 are for fluting ($n = 3$), and the last two columns (M_9 and M_{10}) are for kink overtone.

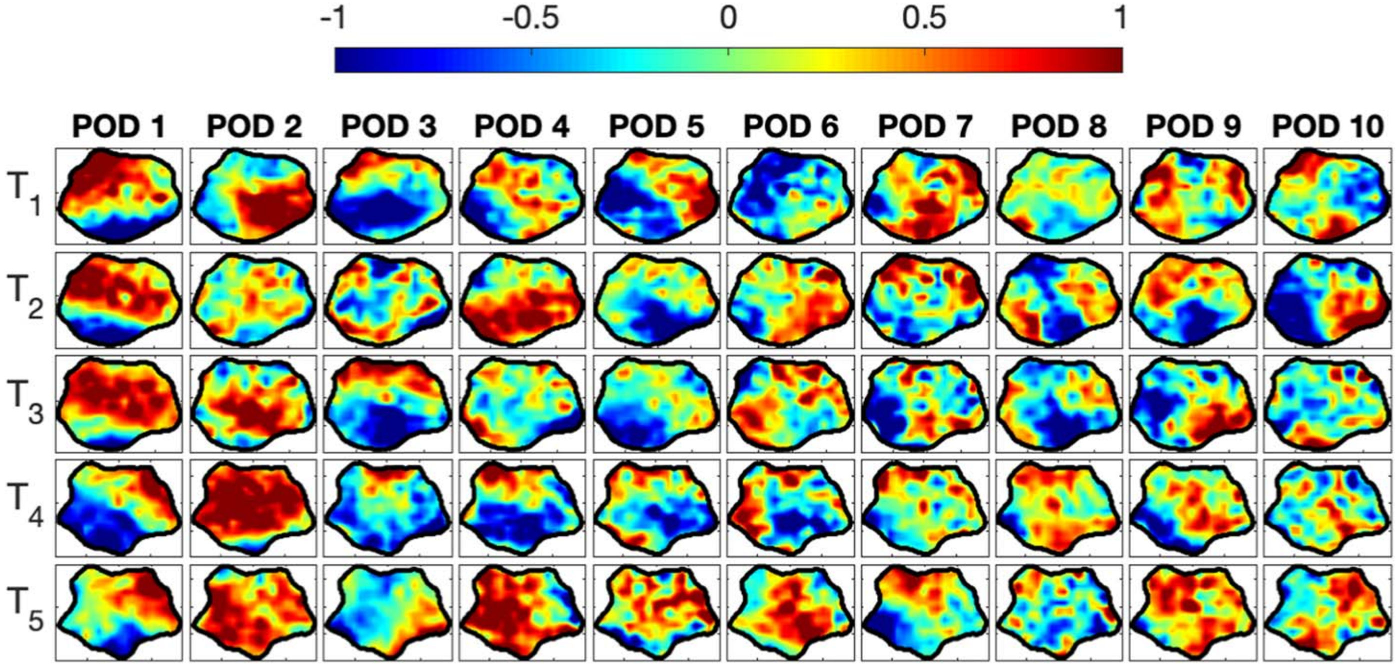

Figure 19. First 10 POD modes of the circular sunspot. Every column shows a POD mode, and the rows show how the modes change at each time interval, T_i, of the data time series. Every time interval contains 80 images and has a duration of 60 minutes. Every time interval is shifted by 40 images, which correponds to 30 minutes.

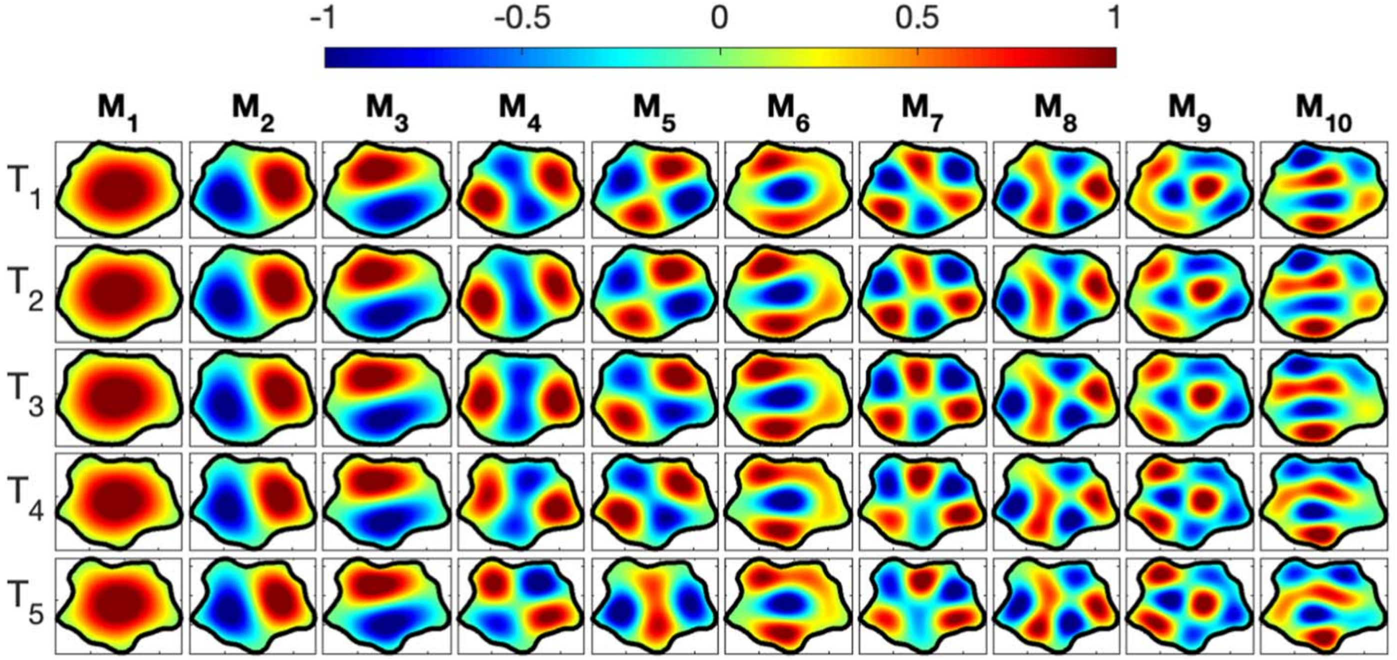

Figure 20. Theoretical eigenfunctions that correspond to the changing shapes of the observed circular sunspot (see Figure 19). M_1 is for fundamental sausage, M_2 and M_3 denote the fundamental kink, M_4 and M_5 are for fluting ($n = 2$), M_6 is for sausage overtone, M_7 and M_8 are for fluting ($n = 3$), and the last two columns (M_9 and M_{10}) are are for kink overtone.

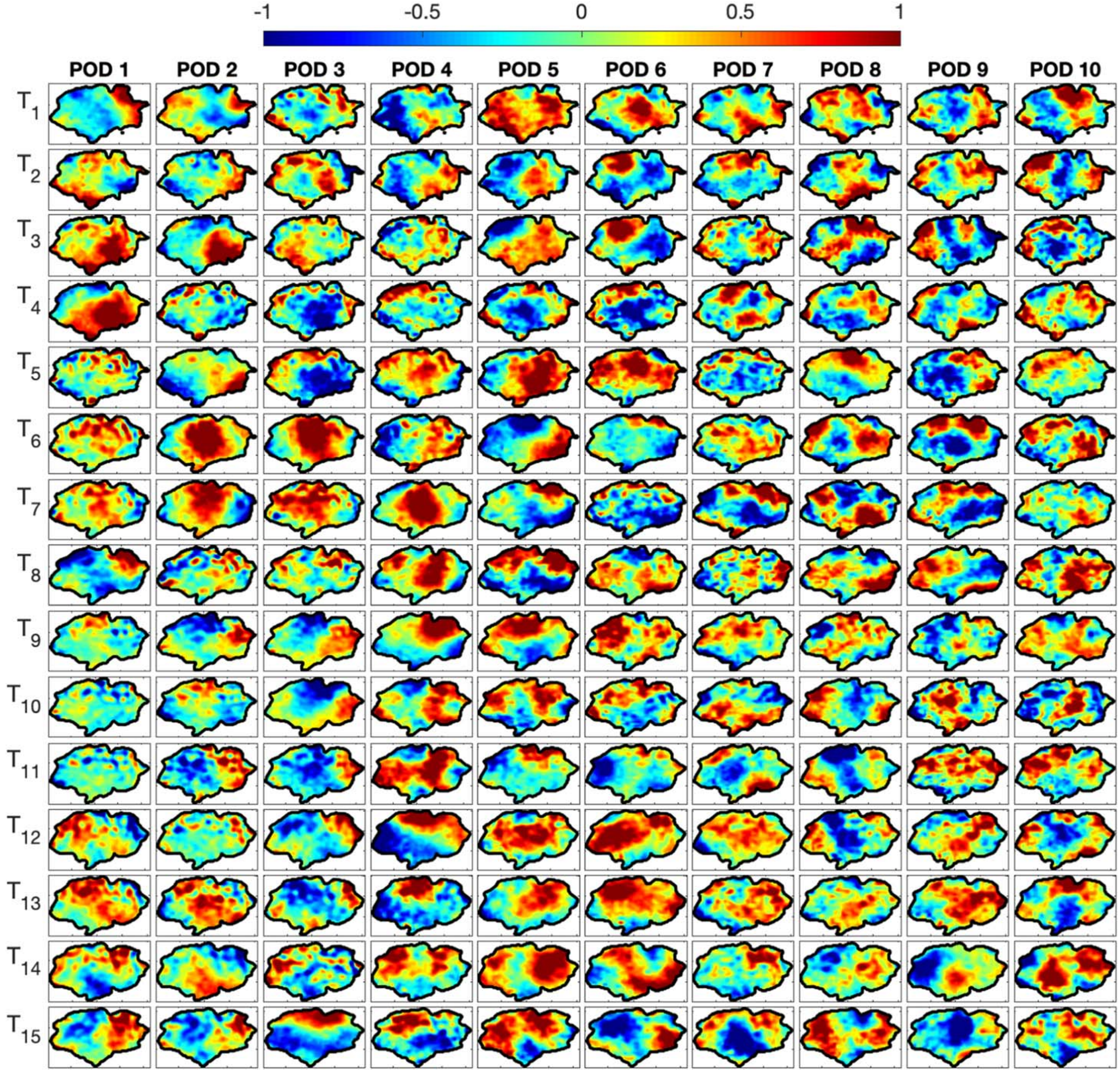

Figure 21. First 10 POD modes of the elliptical sunspot. Every column shows a POD mode, and the rows show how the modes change at each time interval, T_i, of the data time series. Every time interval contains 50 images and has a duration of 37.5 minutes. Every time interval is shifted by 30 images, which correponds to 22.5 minutes.

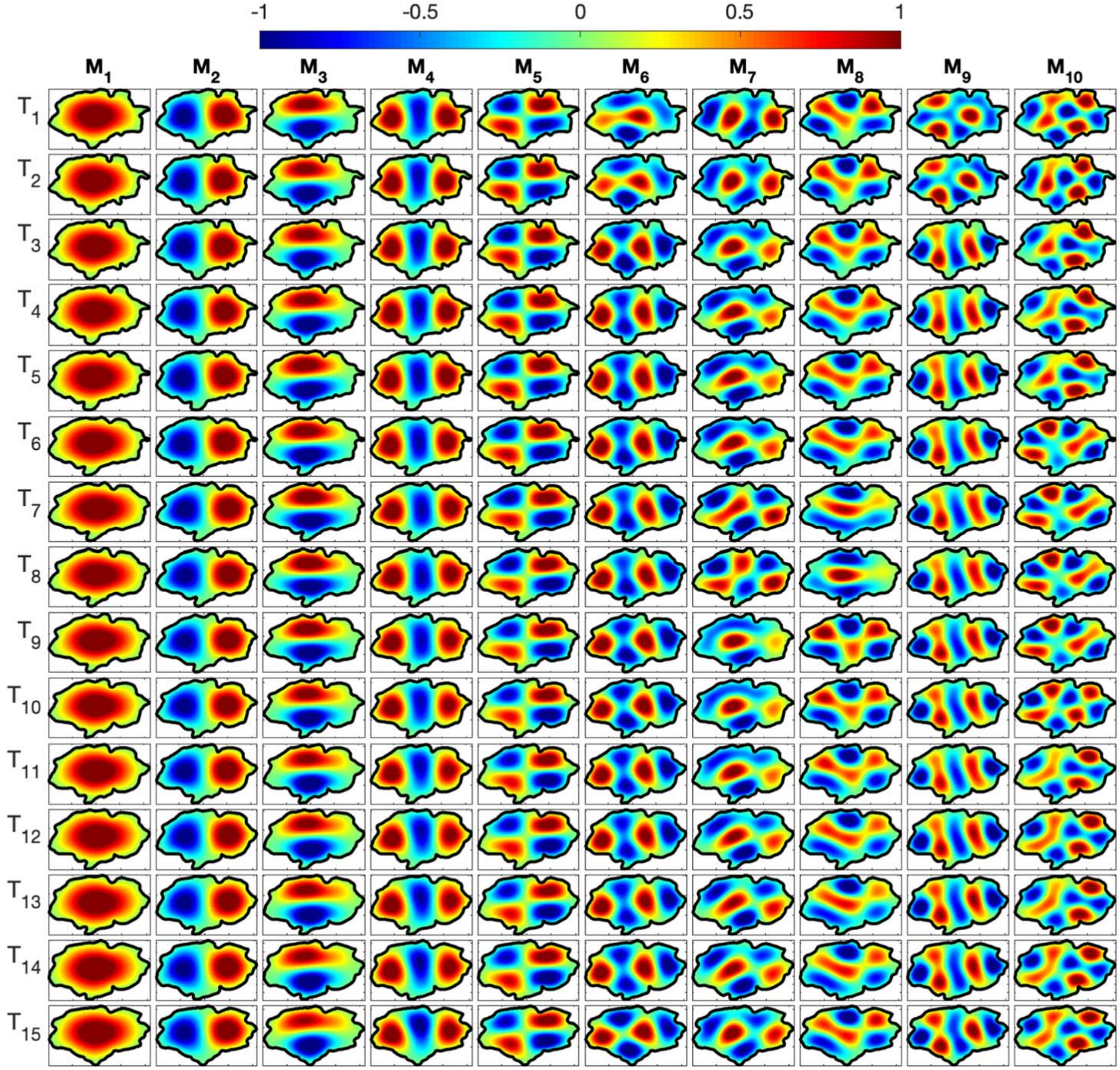

Figure 22. Theoretical eigenfunctions that correspond to the changing shapes of the observed elliptical sunspot (see Figure 21). M_1 is for fundamental sausage, M_2 and M_3 are for fundamental kink, M_4 and M_5 are for fluting ($n = 2$), M_6 is for sausage overtone, M_7 and M_8 are for fluting ($n = 3$), and the last two columns (M_9 and M_{10}) are for kink overtone.

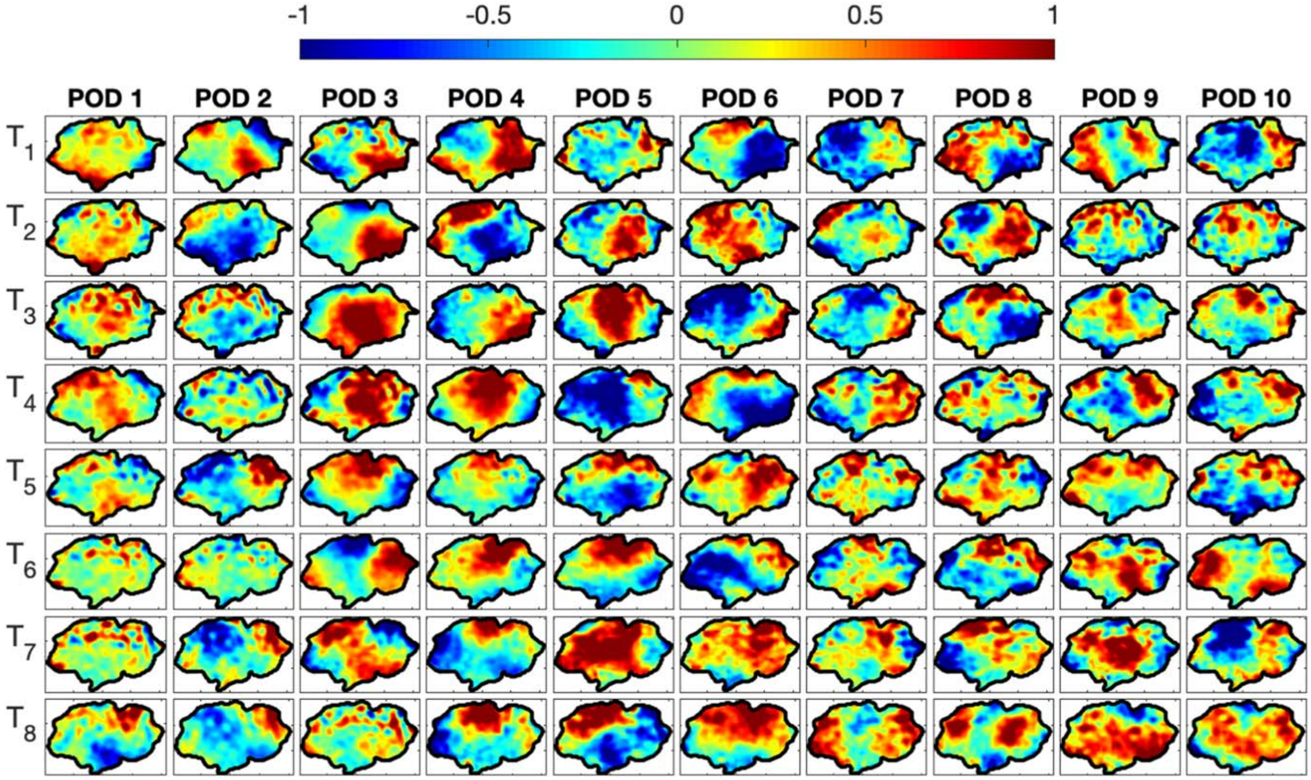

Figure 23. First 10 POD modes of the elliptical sunspot. Every column shows a POD mode, and the rows show how the modes change at each time interval, T_i, of the data time series. Every time interval contains 100 images and has a duration of 75 minutes. Every time interval is shifted by 50 images, which correponds to 37.5 minutes.

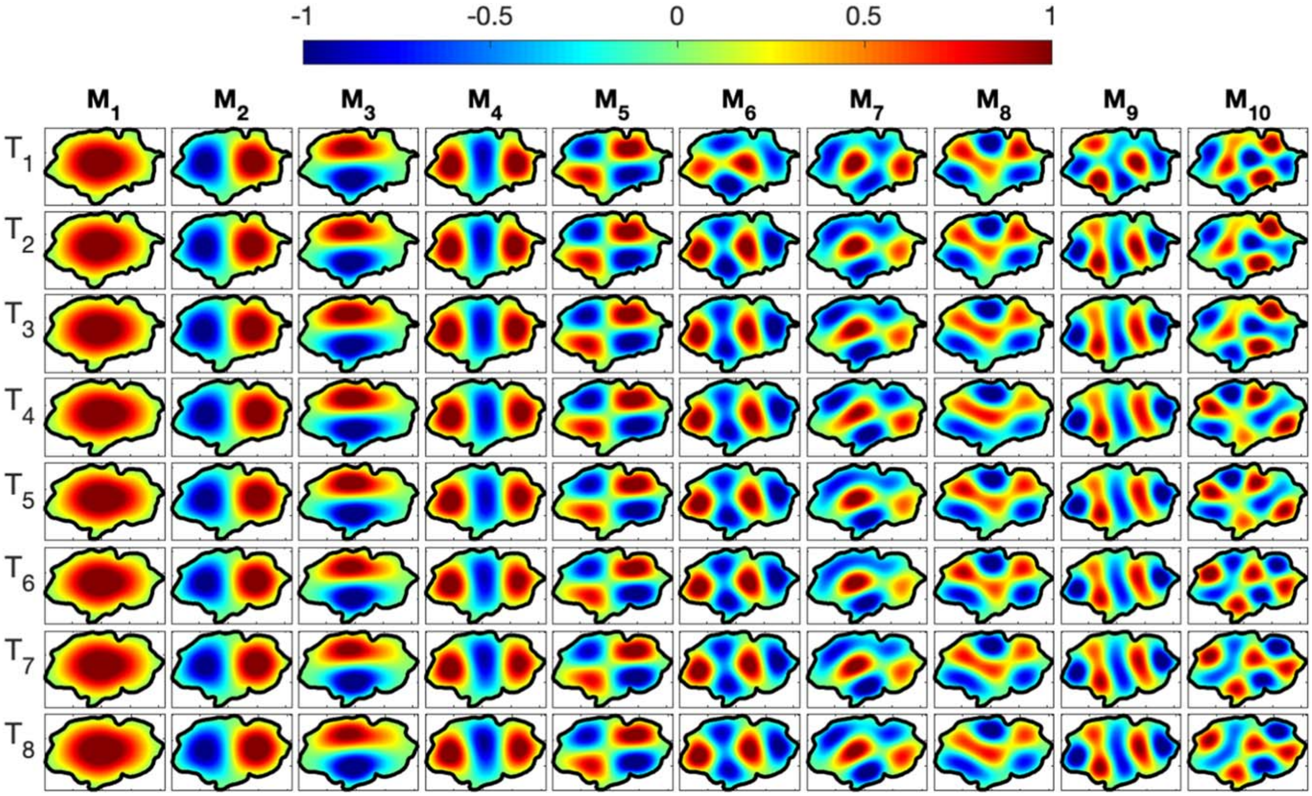

Figure 24. Theoretical eigenfunctions that correspond to the changing shapes of the observed elliptical sunspot (see Figure 23). M_1 is for fundamental sausage, M_2 and M_3 are for fundamental kink, M_4 and M_5 are for fluting ($n = 2$), M_6 is for sausage overtone, M_7 and M_8 are for fluting ($n = 3$), and the last two columns (M_9 and M_{10}) are for kink overtone.

ORCID iDs

A. B. Albidah https://orcid.org/0000-0001-7314-1347
V. Fedun https://orcid.org/0000-0002-0893-7346
A. A. Aldhafeeri https://orcid.org/0000-0003-2220-5042
I. Ballai https://orcid.org/0000-0002-3066-7653
D. B. Jess https://orcid.org/0000-0002-9155-8039
W. Brevis https://orcid.org/0000-0001-8161-4677
J. Higham https://orcid.org/0000-0001-7577-0913
M. Stangalini https://orcid.org/0000-0002-5365-7546
S. S. A. Silva https://orcid.org/0000-0001-5414-0197
C. D. MacBride https://orcid.org/0000-0002-9901-8723
G. Verth https://orcid.org/0000-0002-9546-2368

References

Albidah, A. B., Brevis, W., Fedun, V., et al. 2021, RSPTA, 379, 20200181
Albidah, A. B., Fedun, V., Aldhafeeri, A. A., et al. 2022, ApJ, 927, 201
Aldhafeeri, A. A., Verth, G., Fedun, V., Lennard, M., & Ballai, I. 2022, ApJ, 938, 32
Bagheri, S. 2013, JFM, 726, 596
Berry, M., Magstadt, A., & Glauser, M. N. 2017, PhFl, 29, 020706
Edwin, P., & Roberts, B. 1983, SoPh, 88, 179
Higham, J., Brevis, W., & Keylock, C. 2018, J. Hydraul. Res., 56, 796
Jess, D. B., Morton, R. J., Verth, G., et al. 2015, SSRv, 190, 103
Jess, D. B., Shelyag, S., Mathioudakis, M., et al. 2012, ApJ, 746, 183
Jovanović, M. R., Schmid, P. J., & Nichols, J. W. 2014, PhFl, 26, 024103
Khomenko, E., & Collados, M. 2015, LRSP, 12, 6
Mumford, S. J., Freij, N., Christe, S., et al. 2021, SunPy, v3.0.0, Zenodo, doi:10.5281/zenodo.4762113
Murray, N. E., & Ukeiley, L. S. 2007, ExFl, 42, 79
Nagashima, K., Sekii, T., Kosovichev, A. G., et al. 2007, PASJ, 59, S631
Pearson, K. 1901, London, Edinburgh, Dublin Philos. Mag. J. Sci., 2, 559
Pesnell, W. D., Thompson, B. J., & Chamberlin, P. C. 2011, SoPh, 275, 3
Rowley, C. W., Mezić, I., Bagheri, S., Schlatter, P., & Henningson, D. S. 2009, JFM, 641, 115
Rubio, L. B., Collados, M., Cobo, B. R., & Hidalgo, I. R. 2000, ApJ, 534, 989
Schmid, P. J. 2010, JFM, 656, 5
Schou, J., Scherrer, P. H., Bush, R. I., et al. 2011, SoPh, 275, 229
Stangalini, M., Del Moro, D., Berrilli, F., & Jefferies, S. 2011, A&A, 534, A65
Stangalini, M., Jess, D., Verth, G., et al. 2021, A&A, 649, A169
Stangalini, M., Verth, G., Fedun, V., et al. 2022, NatCo, 13, 479
The SunPy Community, Barnes, W. T., Bobra, M. G., et al. 2020, ApJ, 890, 68